Computer Physics Communications 307 (2025) 109400

Contents lists available at ScienceDirect

Computer Physics Communications

journal homepage: www.elsevier.com/locate/cpc

Computer Programs in Physics

A high-order finite-difference solver for direct numerical simulations of magnetohydrodynamic turbulence ☆

Jian Fang [a,*], Sylvain Laizet [b], Alex Skillen [c]

[a] Scientific Computing Department, Science and Technology Facilities Council, Daresbury Laboratory, Keckwick Lane, Daresbury, Warrington, WA4 4AD, United Kingdom
[b] Department of Aeronautics, Imperial College London, London, SW7 2AZ, United Kingdom
[c] School of Engineering, The University of Manchester, Manchester, M13 9PL, United Kingdom

ARTICLE INFO

Keywords:
Magnetohydrodynamics
High performance computing
High-order finite-difference schemes
Direct numerical simulation

ABSTRACT

This paper presents the development and validation of a Magnetohydrodynamics (MHD) module integrated into the Xcompact3d framework, an open-source high-order finite-difference suite of solvers designed to study turbulent flows on supercomputers. Leveraging the Fast Fourier Transform library already implemented in Xcompact3d, alongside sixth-order compact finite-difference schemes and a direct spectral Poisson solver, both the induction and potential-based MHD equations can be efficiently solved at scale on CPU-based supercomputers for fluids with strong and weak magnetic field, respectively. Validation of the MHD solver is conducted against established benchmarks, including Orszag-Tang vortex and MHD channel flows, demonstrating the module's capability to accurately capture complex MHD phenomena, providing a powerful tool for research in both engineering and astrophysics. The scalability of the Xcompact3d framework remains intact with the incorporation of the MHD module, ensuring efficient performance on modern high-performance clusters. This paper also presents new findings on the evolution of the Taylor-Green vortex under an external magnetic field for different flow regimes.

PROGRAM SUMMARY

Program Title: Xcompact3d

CPC Library link to program files: https://doi.org/10.17632/z835zbbs8g.1

Developer's repository link: https://github.com/Xcompact3d/Xcompact3d

Licensing provisions: BSD 3-Clause License

Programming language: Fortran

Nature of problem: Magnetohydrodynamics.

Solution method: High-order finite-difference method and spectral based Poisson solver.

Additional comments including restrictions and unusual features: Heterogeneous parallel capabilities with GPUs are under active development.

1. Introduction

Magnetohydrodynamics (MHD) involves the study of the dynamics of a flow field coupled with an electromagnetic field. MHD occurs in a wide range of problems with a vast variety of scales, such as plasma arc gasification flow at micro-scales, plasma confinement in nuclear fusion reactors at lab scales, geophysics at planetary scales, and astrophysics at interstellar scales. Simulating accurately MHD flows is generally a challenging task by comparison to simulating pure fluid dynamics. The difficulty arises from the fact both the Navier-Stokes (NS) equations and the Maxwell equations are nonlinear, and the two sets of equations are also often tightly coupled. Experimental investigation of MHD flow is also difficult to conduct due to the opaque nature of liquid metals (preventing the use of traditional optical measurement techniques such as particle image velocimetry). Therefore, numerical simulation is the unavoidable way forward for a better understanding of MHD flows.

☆ The review of this paper was arranged by Prof. David W.Walker.

* Corresponding author.
E-mail addresses: jian.fang@stfc.ac.uk (J. Fang), s.laizet@imperial.ac.uk (S. Laizet), alex.skillen@manchester.ac.uk (A. Skillen).

https://doi.org/10.1016/j.cpc.2024.109400
Received 23 July 2024; Received in revised form 4 October 2024; Accepted 10 October 2024
Available online 15 October 2024

The NS equations are a widely accepted mathematical model for describing turbulent flow motions. However, solving these equations is extremely challenging due to the chaotic and inherently multi-scale nature of turbulence. Turbulent scales typically span several orders of magnitude, necessitating significant computing power and memory for accurate resolution. With the recent dramatic increase in computational resources, high-fidelity simulations of turbulent flows, such as direct numerical simulations (DNS) and large eddy simulations (LES), have become widely used techniques for predicting turbulent flows. Consequently, computational fluid dynamics (CFD) has become a critical complement to experiments and theoretical approaches.

The most accurate approach to turbulence simulations is DNS for which the NS equations are solved without averaging, modelling assumptions and parameterisations (*e.g.*, sub-grid) or approximations other than numerical discretisations. It is also the simplest approach conceptually because all the motions of the flow are resolved in such simulations. DNS are especially important for MHD flows, as MHD turbulence is less understood compared to conventional turbulence; models therefore typically do not exist or are at early stages of development. For instance, it has been demonstrated that the scaling of conventional homogeneous isotropic turbulence (*e.g.*, the classical Kolmogorov K41 scaling [1]) does not hold for MHD turbulence [2–4], and therefore conventional turbulence models tend to mispredict the under-resolved turbulent motion for MHD flows, leading to incorrect results.

The usefulness of highly accurate numerical schemes for DNS/LES in fundamental academic flow configurations is well recognised. For very simplified geometries, the most spectacular gains in terms of accuracy and computational efficiency are achieved using spectral methods based on Fourier or Chebyshev representations [5,6]. Various combinations of these two types of spectral discretisation have enabled numerous authors to efficiently address fundamental turbulent problems in the context of incompressible flows. Examples include homogeneous turbulence (using full Fourier representation), transitional or turbulent channel flow (using mixed Fourier-Chebyshev representation), and turbulence in a cavity (using full Chebyshev representation). The spectral and pseudo-spectral methods have also been extensively applied for the studies of MHD flows. As for DNS/LES of turbulence, the periodic and non-periodic directions are generally discretised with Fourier-based and Chebyshev polynomials-based methods, respectively (see, e.g., the work of Turbulence and Heat Transfer Laboratory (THTLab) at The University of Tokyo [7]). Recently, Fontana et al. [8] introduced the Fourier-based method also to the non-periodic flows using Fourier continuation expansions combined with Gram polynomials, which can enforce zero divergences for both velocity and magnetic fields accurately and efficiently.

However, for fundamental problems involving slightly more complex geometries, a full spectral approach in Fourier or Chebyshev space is not suitable. Despite recent progress in CFD methods, the use of sophisticated meshes combined with high-order schemes remains challenging, requiring significant numerical development to achieve both accuracy and efficiency.

A favourable combination of numerical methods and computational techniques to study turbulent flows is based on high-order finite-difference schemes with an accuracy preserved through the use of a regular computational mesh. Such an approach can be seen as an intermediate strategy between fully spectral NS solvers for academic geometry (Fourier/ Chebyshev representation) and more versatile codes based on standard numerical schemes of lower accuracy. Such high-order schemes provide a good spectral resolution at high wavenumbers with low dissipative properties at all wavenumbers; this allows the resolution of small-scale flow structures efficiently while minimising numerical errors [9,10].

Compared to conventional turbulence, DNS of MHD turbulence has a high requirement on numerical methods. First, the number of equations for MHD turbulence is twice that of the NS equations. Second, the solver should enforce a divergence-free condition on the magnetic field to be within the limit of machine round-off error to prevent the spurious generation of unphysical magnetic monopoles. Third, the magnetic structures from MHD turbulence have the potential to be much smaller than flow structures in conventional turbulence. Therefore, DNS of MHD turbulence has a higher requirement on the mesh spacing, numerical accuracy and efficiency of the solver.

In this paper, we present an MHD solver based on a Fortran 90-95 open-source CFD framework, Xcompact3d [11], targeting CPU-based supercomputers. It is an evolution the flow solver Incompact3d which was initially designed in France in the mid-90's for serial processors to solve the incompressible NS equations. The pressure Poisson equation is solved directly in spectral space via the use of three-dimensional (3D) Fast Fourier Transforms [10]. The parallelisation of Xcompact3d is achieved through the 2DECOMP&FFT library [12] to leverage the computational resources of the latest generations of supercomputers.

The high numerical accuracy and computational performance of Xcompact3d provides a good platform for developing a high-order DNS solver to study and analyse MHD flows.

The paper is organised as follows: the governing equations and the details of the implementation of the MHD module in Xcompact3d are presented in Section 2. The validation of the MHD module against established benchmarks is then conducted in Section 3. Section 4 is dedicated to the study of the 3D Taylor-Green vortex flow with an enforced magnetic field with a strong kinetics/magnetism interaction. Summary and concluding remarks are given in Section 5.

2. Governing equations and implementation

2.1. Governing equations

For an incompressible flow involving electromagnetic fields, the primitive variables to solve generally include the velocity field, $\vec{u} = (u_x, u_y, u_z)$, and the magnetic field, $\vec{B} = (B_x, B_y, B_z)$. The governing equations for the velocity and magnetic fields are given in a non-dimensional form respectively as,

$$\frac{\partial \vec{u}}{\partial t} = -\frac{1}{2}\left[(\vec{u}\cdot\nabla)\vec{u} + \nabla\cdot(\vec{u}\otimes\vec{u})\right] - \nabla p + \frac{1}{\mathrm{Re}}\nabla^2\vec{u} + \mathrm{N}\left(\vec{J}\times\vec{B}\right), \tag{1}$$

$$\frac{\partial \vec{B}}{\partial t} = \frac{1}{2}\left[\left(\vec{B}\cdot\nabla\right)\vec{u} + \nabla\left(\vec{B}\otimes\vec{u}\right)\right] - \frac{1}{2}\left[(\vec{u}\cdot\nabla)\vec{B} + \nabla\left(\vec{u}\otimes\vec{B}\right)\right] + \frac{1}{\mathrm{Re}_\mathrm{m}}\nabla^2\vec{B}, \tag{2}$$

where p is the pressure and $\vec{J}$ is the current density vector. The Reynolds number, $\mathrm{Re} = UL/\nu$, dictates the ratio between inertial and viscous forces, in which, U, L and ν are respectively the reference velocity, reference length and kinematic viscosity. The magnetic Reynolds number, $\mathrm{Re_m} = UL/\eta$, indicates the ratio between magnetic induction to diffusion. The magnetic diffusivity η is calculated as $\eta = 1/\mu\sigma$, in which μ is the magnetic permeability, and σ is the electric conductivity. The Stuart number, N, also known as the magnetic interaction parameter, is defined as the ratio of electromagnetic to inertial forces, $\mathrm{N} = \sigma B_0^2 L/\rho_0 U$, in which B_0 is the reference magnetism, ρ_0 is the reference density of the fluid. The symbol, $\otimes$, stands for the outer production operation.

Eq. (1) is the Navier–Stokes momentum equation with an extra Lorentz force term, $\mathrm{N}\left(\vec{J}\times\vec{B}\right)$. Eq. (2) is the magnetic induction equation, arising from the combination of Ohm's and Ampere's laws. The two transport equations are nonlinearly coupled. The conservation of mass requires velocity field satisfies,

$$\nabla\cdot\vec{u} = 0, \tag{3}$$

and the magnetic field also needs to satisfy the Gauss' law for magnetism:

$$\nabla\cdot\vec{B} = 0. \tag{4}$$

Both the convective terms in the momentum and magnetic equations are written in the skew-symmetric form to reduce aliasing errors from solving these equations numerically [13–15]. For the sake of clarity, the convective terms in Eq. (2) are expanded as follows,

$$
\begin{aligned}
\left(\vec{B}\cdot\nabla\right)\vec{u} &= \begin{pmatrix} B_x\frac{\partial u_x}{\partial x}+B_y\frac{\partial u_x}{\partial y}+B_z\frac{\partial u_x}{\partial z} \\ B_x\frac{\partial u_y}{\partial x}+B_y\frac{\partial u_y}{\partial y}+B_z\frac{\partial u_y}{\partial z} \\ B_x\frac{\partial u_z}{\partial x}+B_y\frac{\partial u_z}{\partial y}+B_z\frac{\partial u_z}{\partial z} \end{pmatrix}, \\
\nabla\left(\vec{B}\otimes\vec{u}\right) &= \begin{pmatrix} \frac{\partial B_x u_x}{\partial x}+\frac{\partial B_y u_x}{\partial y}+\frac{\partial B_z u_x}{\partial z} \\ \frac{\partial B_x u_y}{\partial x}+\frac{\partial B_y u_y}{\partial y}+\frac{\partial B_z u_y}{\partial z} \\ \frac{\partial B_x u_z}{\partial x}+\frac{\partial B_y u_z}{\partial y}+\frac{\partial B_z u_z}{\partial z} \end{pmatrix}, \\
\left(\vec{u}\cdot\nabla\right)\vec{B} &= \begin{pmatrix} u_x\frac{\partial B_x}{\partial x}+u_y\frac{\partial B_x}{\partial y}+u_z\frac{\partial B_x}{\partial z} \\ u_x\frac{\partial B_y}{\partial x}+u_y\frac{\partial B_y}{\partial y}+u_z\frac{\partial B_y}{\partial z} \\ u_x\frac{\partial B_z}{\partial x}+u_y\frac{\partial B_z}{\partial y}+u_z\frac{\partial B_z}{\partial z} \end{pmatrix}, \\
\nabla\left(\vec{u}\otimes\vec{B}\right) &= \begin{pmatrix} \frac{\partial u_x B_x}{\partial x}+\frac{\partial u_y B_x}{\partial y}+\frac{\partial u_z B_x}{\partial z} \\ \frac{\partial u_x B_y}{\partial x}+\frac{\partial u_y B_y}{\partial y}+\frac{\partial u_z B_y}{\partial z} \\ \frac{\partial u_x B_z}{\partial x}+\frac{\partial u_y B_z}{\partial y}+\frac{\partial u_z B_z}{\partial z} \end{pmatrix}.
\end{aligned}
\tag{5}
$$

The current density vector, $\vec{J}$, is obtained from the Ampere's law, closing the system:

$$
\vec{J}=\frac{1}{\mathrm{Re_m}}\nabla\times\vec{B} \tag{6}
$$

For cases with a low magnetic Reynolds number, $\mathrm{Re_m}\ll 1$, the magnetic field is decoupled from the velocity field, and determined by the boundary conditions. Therefore, the induced magnetic field can be neglected, and the magnetic field can be seen as a time-invariant field as, $\vec{B}=\vec{B}_0$. By employing Ohm's law, a Poisson equation for the electric potential, φ, can be obtained as,

$$
\nabla^2\varphi=\nabla\cdot\left(\vec{u}\times\vec{B}\right), \tag{7}
$$

and the current density distribution can be expressed by,

$$
\vec{J}=-\nabla\varphi+\vec{u}\times\vec{B}. \tag{8}
$$

In summary, one of two systems of governing equations can be used to solve a MHD problem, depending on the magnetic Reynolds number:

- For a flow with relatively high $\mathrm{Re_m}$, Eqs. (1) and (2) are solved to obtain the velocity and magnetic fields, combining the divergence-free constraints for both fields, Eqs. (3) and (4). The current density is calculated from the magnetic field via Eq. (6).
- For a flow with $\mathrm{Re_m}\ll 1$, and $\vec{B}=\vec{B}_0$, we can still solve Eq. (1) with constraint Eq. (3) to obtain the velocity field. Instead of solving the induction equation, Eq. (2), we can choose to solve the electric potential equation, Eq. (7), and further calculate $\vec{J}$ via Eq. (8).

In this study, the two solvers are named the induction solver and the potential solver, respectively. The first system of equations is normally used in plasma flow and astrophysics, where the magnetic field is highly dynamic and changes with time. The latter system is widely used in lab-scale MHD such as in liquid metal flows relevant to nuclear fusion, where the magnetic field is applied to fluids from an external source and the induced magnetic field is negligible. From the computational point of view, the second system of equations is more efficient to solve; as the number of equations to solve is lower than the first system, and Eq. (2) tends to be numerically stiff with a very low $\mathrm{Re_m}$, making its solution impractical for many lab-scale MHD problems.

Table 1
The input parameters for the MHD module in Xcompact3d.

MHD parameter	Description
`mhd_active`	Logical variable to active the MHD module
`mhd_equation`	String to select the MHD system to solve:
	`induction` to select Eq. (2).
	`potential` to select Eq. (7)
`hartmann`	Float variable for Hartmann number
`stuart`	Float variable for Stuart number
`rem`	Float variable for magnetic Reynolds
	number (only for `mhd_equation` equal to '`induction`')

2.2. Implementation procedure

A new MHD module is developed within the framework of Xcompact3d, and a set of input parameters are added into input files, to parameterise the MHD module, as listed in Table 1.

Both the induction solver and the potential solver are included in the MHD module of Xcompact3d, and the users can select one of them by editing the value of the variable, `mhd_equation`, in the input file. The comparison of the computational loops among the original NS solver, the induction solver with the magnetic induction equations, and the potential solver with the electric potential equitation is presented in Fig. 1.

To solve the NS equations in Xcompact3d, the first step is to calculate the convection and the diffusion terms, *i.e.*, the terms, $\frac{1}{2}\left[\left(\vec{u}\cdot\nabla\right)\vec{u}+\nabla\cdot\left(\vec{u}\otimes\vec{u}\right)\right)$, and $\frac{1}{\mathrm{Re}}\nabla^2\vec{u}$, in Eq. (1), with the first- and second-derivatives being calculated via sixth-order compact finite-difference schemes on a collocated Cartesian mesh. The intermediate velocity field, $\vec{u}^*$, can then be obtained by advancing Eq. (1) in time using a fractional step method, but this intermediate velocity field is, in general, not divergence-free. Time advancement is performed using an explicit high-order Adams-Bashforth scheme or Runge-Kutta scheme. The next step is to correct this velocity field with the pressure gradients. The pressure Poisson equation,

$$
\nabla^2 p=\nabla\cdot\vec{u}^*, \tag{9}
$$

is solved in the Fourier space to obtain a pressure field, and the velocity is then projected onto a divergence-free space using the pressure gradient,

$$
\vec{u}=\vec{u}^*-\nabla p. \tag{10}
$$

When the parameter `mhd_equation` is set to '`induction`', the induction equations are solved via a similar procedure, as shown Fig. 1 (b). The convection and diffusion terms in Eq. (2) are first solved using a sixth-order compact finite-difference method, and the intermediate magnetic field, $\vec{B}^*$, is obtained through time integration. To ensure a divergence-free magnetic field, we incorporate the divergence cleaning technique proposed by Dedner et al. [16], in which a virtual magnetic pressure term, ψ, is introduced to Eq. (2) as,

$$
\begin{aligned}
\frac{\partial\vec{B}}{\partial t}+\nabla\psi=&\frac{1}{2}\left[\left(\vec{B}\cdot\nabla\right)\vec{u}+\nabla\left(\vec{B}\otimes\vec{u}\right)\right] \\
&-\frac{1}{2}\left[\left(\vec{u}\cdot\nabla\right)\vec{B}+\nabla\left(\vec{u}\otimes\vec{B}\right)\right]+\frac{1}{Re_m}\nabla^2\vec{B}.
\end{aligned}
\tag{11}
$$

The magnetic Poisson equation is then incorporated to solve ψ,

$$
\nabla^2\psi=\nabla\cdot\vec{B}^*, \tag{12}
$$

and a divergence-free magnetic field at the new time step is then obtained through a projection step as,

$$
\vec{B}=\vec{B}^*-\nabla\psi. \tag{13}
$$

The current density field, $\vec{J}$, can subsequently be calculated from $\vec{B}$ using Eq. (6), and the force term, $N\left(\vec{J}\times\vec{B}\right)$, is obtained and applied to

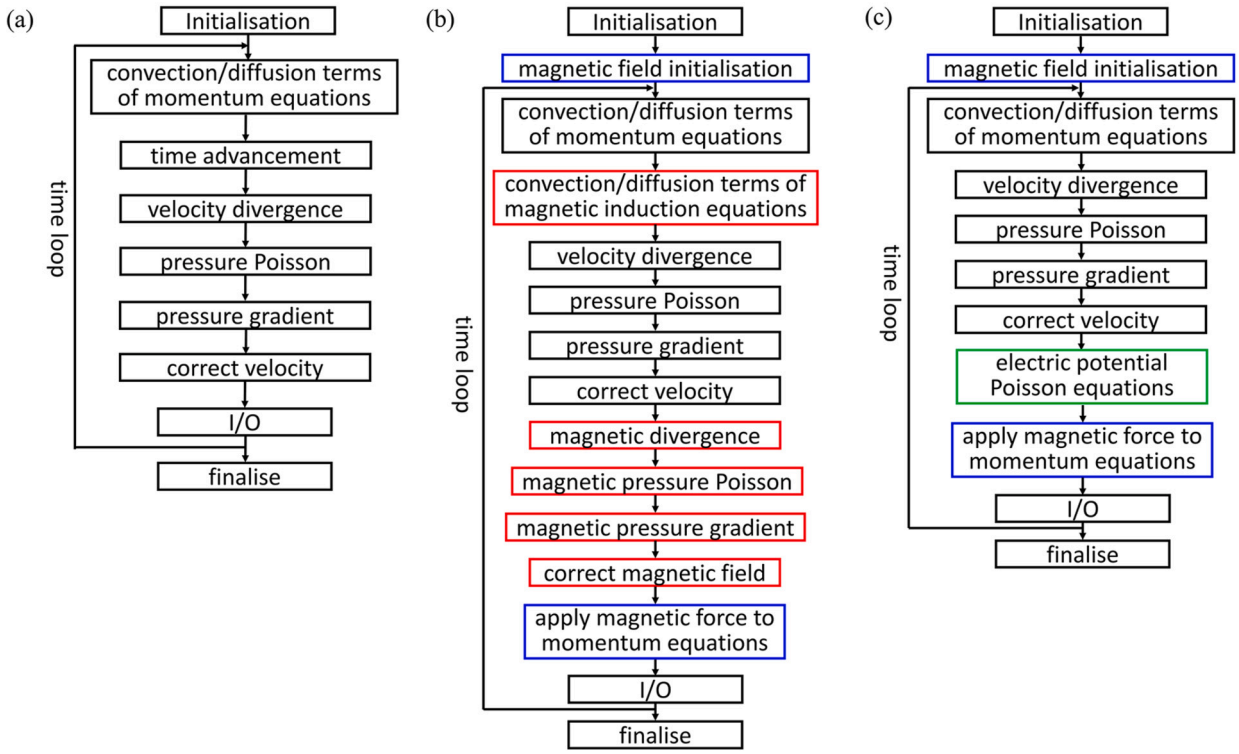

Fig. 1. The computational loops of (a): the NS solver (`mhd_active` set to false), (b): the induction solver, and (c): the potential solver. The blue boxes indicate the common MHD routines; the red boxes are the routines related to the induction equations; the green box is the routine that solves the potential equation. (For interpretation of the colours in the figure(s), the reader is referred to the web version of this article.)

the momentum equation, Eq. (1), to finalise a loop of solving the MHD system.

When the parameter `mhd_equation` is set to '`potential`', the computational procedure for MHD is comparatively simpler, as shown in Fig. 1 (c). Given a known magnetic field, $\vec{B} = \vec{B}_0$, only one Poisson equation for the electric potential, Eq (7), needs to be solved. The current density field is calculated using Eq. (8), and the magnetic force term is applied to the momentum equations in the same way as above.

2.3. Numerical details

Xcompact3d is based on a Cartesian mesh and uses finite-difference sixth-order compact (implicit) schemes for spatial discretisation. The main originality of Xcompact3d is that the Poisson equation for the incompressibility of the velocity field is fully solved in spectral space via the use of relevant 3D Fast Fourier transforms (FFTs).

With the help of the concept of modified wavenumber [9], the divergence free condition is ensured up to machine accuracy. The simplicity of the mesh allows an easy implementation of a two-dimensional (2D) domain decomposition based on pencils [17]. The computational domain is split into a number of sub-domains (pencils) which are each assigned to an MPI-process. The derivatives and interpolations in the x-direction (y-direction, z-direction) are performed in X-pencils (Y-pencils, Z-pencils), respectively. The 3D FFTs required by the Poisson solver are also broken down as series of 1D FFTs computed in one direction at a time. Global transpositions to switch from one pencil to another are performed with the MPI command `MPI_ALLTOALL(V)`. Xcompact3d can scale well with up to hundreds of thousands MPI-processes for simulations with several billion mesh nodes [17]. The same numerical methods are used for to compute the solution of the MHD equations.

In Xcompact3d, the Poisson equations (*e.g.* Eqs. (9), (7) and (12)), are solved in spectral space using a half-staggered arrangement. For the current MHD module, the velocity field and magnetic field are stored on the main mesh, while the pressure and magnetic pressure are stored on a half staggered mesh with respect to the main mesh. The advantage of using staggered mesh is its numerical stability, see [10].

For simplicity, the procedure of solving a general two-dimensional (2D) Poisson equation,

$$\nabla^2 f = \frac{\partial g}{\partial x} + \frac{\partial h}{\partial y}, \tag{14}$$

with f located on the main velocity mesh, and g and h stored on the half-staggered pressure mesh, can be described as follows:

- The x-derivative term on the right-hand-side of Eq. (14) is first approximated from the main mesh to the half-staggered mesh using the sixth-order compact central scheme for staggered meshes,

$$\begin{aligned}&\frac{9}{62}\frac{\partial g}{\partial x}\bigg|_{i-\frac{1}{2},j} + \frac{\partial g}{\partial x}\bigg|_{i+\frac{1}{2},j} + \frac{9}{62}\frac{\partial g}{\partial x}\bigg|_{i+\frac{3}{2},j}\\ &= 63\frac{g_{i+1,j}-g_{i,j}}{62\Delta x} + 17\frac{g_{i+2,j}-g_{i-1,j}}{186\Delta x},\end{aligned} \tag{15}$$

- An interpolation procedure is conducted for $\frac{\partial g}{\partial x}$ from the half-staggered mesh to the main mesh along the y-direction using a sixth-order midpoint interpolation scheme,

$$\begin{aligned}&\frac{3}{10}\frac{\partial g}{\partial x}\bigg|_{i+\frac{1}{2},j-\frac{1}{2}} + \frac{\partial g}{\partial x}\bigg|_{i+\frac{1}{2},j+\frac{1}{2}} + \frac{3}{10}\frac{\partial g}{\partial x}\bigg|_{i+\frac{1}{2},j+\frac{3}{2}}\\ &= 3\frac{\frac{\partial g}{\partial x}\big|_{i+\frac{1}{2},j+1} + \frac{\partial g}{\partial x}\big|_{i+\frac{1}{2},j}}{4} + \frac{\frac{\partial g}{\partial x}\big|_{i+\frac{1}{2},j+2} + \frac{\partial g}{\partial x}\big|_{i+\frac{1}{2},j-1}}{20}.\end{aligned} \tag{16}$$

- Following the same principle, the y-derivative term can be first calculated from the main mesh to the half-staggered mesh along the y-direction, and then interpolated to main mesh along the x-direction.
- After the variables on both sides of Eq. (14) are evaluated on the main mesh, classic FFT-based Poisson solvers [18–20] can be used to solve Eq. (14).

Table 2
The parameters for the 2D OTV case. The reference velocity, length, and magnetism are equal to 1 in the simulations.

Parameter	Value
`mhd_active`	`true`
`mhd_equation`	`induction`
Stuart number	50
Magnetic Reynolds number	50
Reynolds number	50

It should be noted that the spectral Poisson solver used in Xcompact3d is compatible with non-periodic boundary conditions with the use of cosine Fourier transforms, as explained in [10].

3. Validations and discussions

In this section, the MHD module is validated with a series of canonical MHD flows using the induction equations or the potential equations. The computational time and parallel efficiency of the module is also presented in this section with the analysis of the weak and strong scaling of Xcompact3d with and without the MHD module on a CPU-based supercomputer. Unless otherwise noted, all the benchmark cases are based on the sixth-order compact finite-differences schemes and the FFT-based spectral solver described in the previous section, and a third-order Runge-Kutta scheme [21] for the time integration.

3.1. Two-dimensional Orszag-Tang vortex

The first benchmark case is the 2D Orszag-Tang vortex (OTV) flow, proposed by Orszag and Tang [22], which describes the temporal evolution of initial vortical structures in a $2\pi^2$ square domain with periodic boundary conditions. The flow becomes increasingly complicated due to the nonlinear interaction between velocity and magnetic fields. The initial field is given as,

$$\begin{pmatrix} u_x \\ u_y \\ u_z \end{pmatrix} = 2\begin{pmatrix} -\sin(y) \\ \sin(x) \\ 0 \end{pmatrix}, \begin{pmatrix} B_x \\ B_y \\ B_z \end{pmatrix} = 2\begin{pmatrix} -\sin(y) \\ \sin(2x) \\ 0 \end{pmatrix}. \tag{17}$$

The Magnetic Reynolds number is sufficiently large ($\mathrm{Re_m} = 50$) so that the induction equations have to be solved. The full set of the parameters for this benchmark is listed in Table 2.

The case is simulated with various computational meshes ranging from 32^2 to 256^2 mesh nodes, and the simulations are conducted up to the non-dimensional time, $t = 2$, with a constant time step, $\Delta t = 0.0001$. The vorticity strength, $|\omega_z| = \left|\frac{\partial u_y}{\partial x} - \frac{\partial u_x}{\partial y}\right|$, and the current density, J_z, obtained by using 256^2 mesh nodes, are shown in Figs. 2 and 3, respectively.

Thin sheet-like vortical and electrical structures with large gradients evolve from simple initial fields. This is different from a 2D pure hydrodynamic vortical flow, in which the vortices decay monotonically with time due to the lack of vortex stretching in the third direction [23]. Both the vortical and electrical structures obtained with Xcompact3d agree well quantitatively with the results from previous studies [16,24,25].

The effectiveness of the correction step described in Eq. (12) and (13) is demonstrated by showing the magnetic divergence at $t = 0.6$ in Fig. 4. Before the correction step, the error of magnetic divergence shows high values around the current sheet structures, and after the correction step, the magnetic divergence field has a clear random pattern with noises of order 10^{-13}; close to machine round-off error (the simulations presented in this study are performed in double precision).

The quantitative validation of the evolution of the spatially averaged kinetic/magnetic energy and kinetic/magnetic enstrophy is presented in Fig. 5, in which the kinetic energy, E_k, kinetic enstrophy, Ω_k, magnetic energy, E_n, and magnetic enstrophy, Ω_m, are defined as,

$$E_k(\vec{x},t) = \frac{1}{2}\left(\vec{u}\cdot\vec{u}\right), \quad \Omega_k(\vec{x},t) = \frac{1}{2}\left(\vec{\omega}\cdot\vec{\omega}\right),$$
$$E_m(\vec{x},t) = \frac{1}{2}\left(\vec{B}\cdot\vec{B}\right), \quad \Omega_m(\vec{x},t) = \frac{1}{2}\left(\vec{J}\cdot\vec{J}\right), \tag{18}$$

where the vorticity is defined as

$$\vec{\omega} = \nabla\times\vec{u}. \tag{19}$$

From Fig. 5 (a) we can observe the non-monotonic evolutions of E_k and E_m. The kinetic energy first decays, reaching its minimal value at $t = 1.2$, and then starts to grow. The magnetic energy initially rises, reaching its maxima at $t = 1.0$, and then decays. The total energy presents a monotonic decay, similar to the evolution of kinetic energy in a pure hydrodynamics Taylor-Green vortex flow. The kinetic energy is converted into magnetic energy during the first half of the evolution, afterwards, the magnetic energy is covered back into kinetic energy.

It can be confirmed from Fig. 5 (a) that the results from Xcompact3d agree well with the reference data from previous DNS of Orszag and Tang [5], even for the case with a coarse mesh (*e.g.*, 32^2 mesh nodes). The kinetic/magnetic energies obtained by Xcompact3d with different mesh resolutions collapse well with each other and with the reference data.

The temporal evolution of the enstrophy is more sensitive to the simulation's resolution. According to Fig. 5 (b), the magnetic enstrophy is mesh independent when the mesh size is bigger than 128^2 mesh nodes. The rapid amplification of the magnetic enstrophy is accompanied with the formation of sheet-like structures with strong gradients as shown in Fig. 3. The magnetic enstrophy reaches its maximal value at around $t = 1.0$, when the magnetic energy starts to be converted back into kinetic energy. A good agreement between the present DNS and the data of Orszag and Tang [5] can be observed in Fig. 5 (b) for the time evolution of the kinematic and magnetic enstrophy.

To further assess the results, the global maximums of vorticity and enstrophy at $t = 0.5$ and $t = 1.0$ are compared with the DNS of Dellar [16] and the results of De Rosis et al. [25] in Table 3. It can be seen from Table 3 that our results converge with lower spatial resolution than the reference data, indicating the advantage of using high-order methods for DNS of MHD flows.

3.2. Three-dimensional Orszag-Tang vortex

Following the 2D OTV flow, a 3D OTV case is established by allowing fluctuations in the z-direction within a $2\pi^3$ cubic computational domain (periodic boundary conditions). The initial conditions for the velocity and magnetic fields are given as,

$$\begin{pmatrix} u_x \\ u_y \\ u_z \end{pmatrix} = 2\begin{pmatrix} -\sin(y) \\ \sin(x) \\ 0 \end{pmatrix}, \begin{pmatrix} B_x \\ B_y \\ B_z \end{pmatrix} = 0.8\begin{pmatrix} -2\sin(y)+\sin(z) \\ 2\sin(2x)+\sin(z) \\ \sin(x)+\sin(y) \end{pmatrix}, \tag{20}$$

and the input parameters are listed in Table 4. The 3D simulations are conducted up to the non-dimensional time, $t = 2$, with a constant time step, $\Delta t = 0.0001$ and with mesh sizes ranging from 32^3 to 256^3 mesh nodes.

The temporal evolution of energy is shown in Fig. 6 (a), from which we can see the collapse of all the curves from the different meshes, meaning the results are mesh independent for these quantities. The conversion between kinetic and magnetic energies can also be seen, and the total energy presents a monotonic decay with time. To better illustrate the difference among the results, we calculate the relative errors with respect to the fine mesh result obtained with 256^3 mesh nodes in Fig. 6 (b). The error of the kinetic energy from the simulation with 32^2 mesh nodes is less than 4% and the error quickly reduces with the mesh refinement. When the mesh is refined to 128^3 mesh nodes, the level of errors reduces to approximately 10^{-4}.

The temporal evolution of enstrophy is shown in Fig. 7, and we can see a lower level of magnetic enstrophy resolved for the simulation with 32^3 mesh nodes. Other than that, the collapse for the other simulations

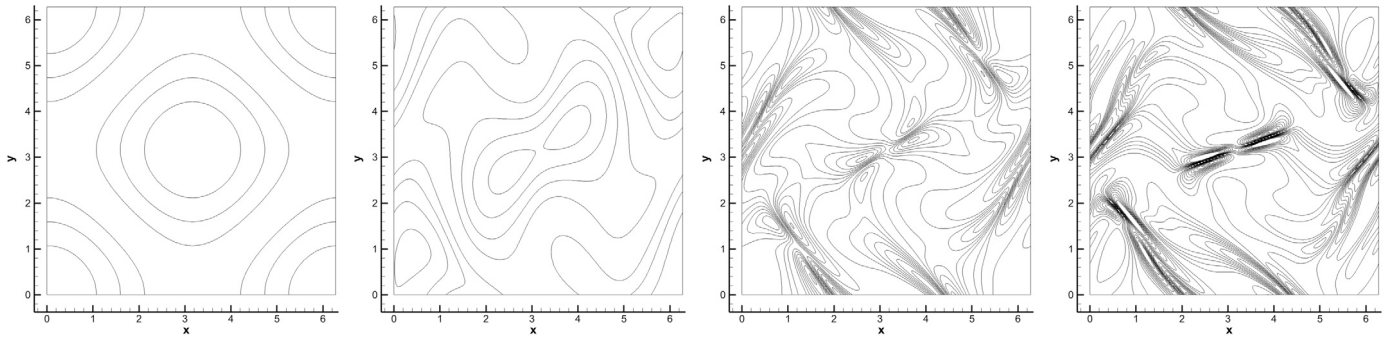

(a) t=0 (b) t=0.2 (c) t=0.6 (d) t=0.85

Fig. 2. Vorticity at different instants for the 2D OTV, represented by 11 contour lines ranging from $|\omega_z| = 0$ to 10.

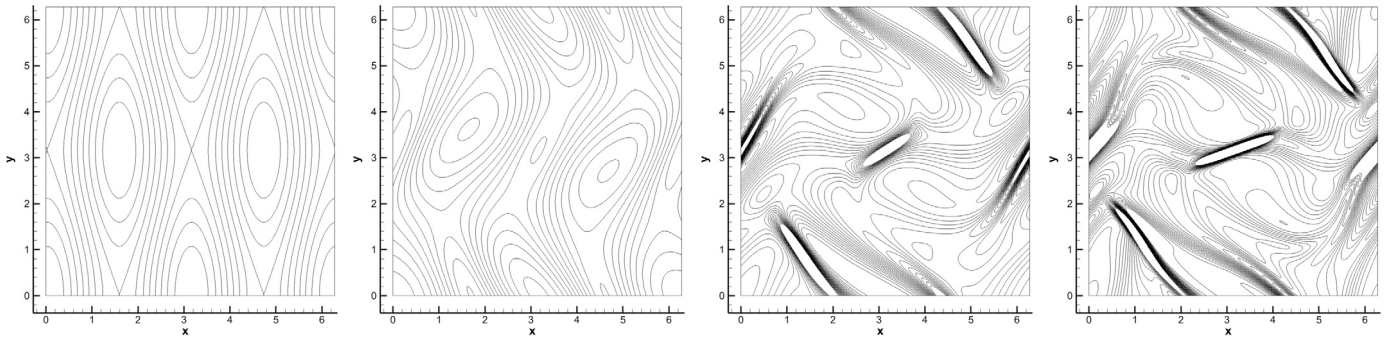

(a) t=0 (b) t=0.2 (c) t=0.6 (d) t=0.85

Fig. 3. Current density at different instants for the 2D OTV, represented by 21 contour lines ranging from $J_z = -0.2$ to 0.2.

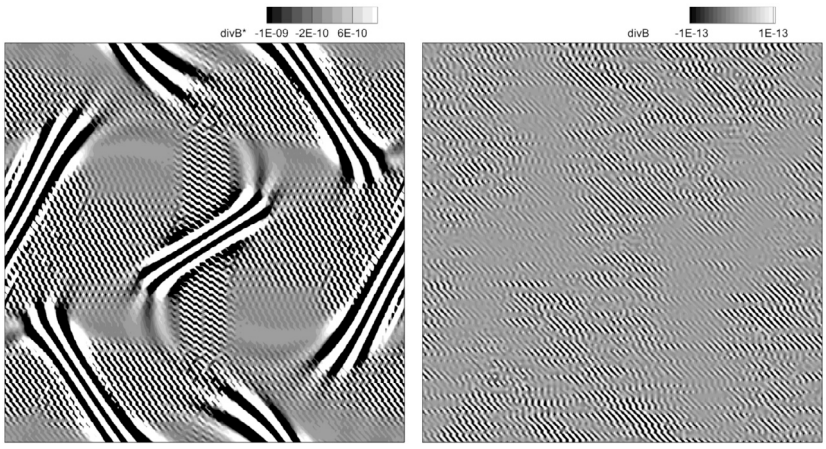

(a) before correction (b) after correction

Fig. 4. Divergence of magnetic field before and after the correction step at $t = 0.6$.

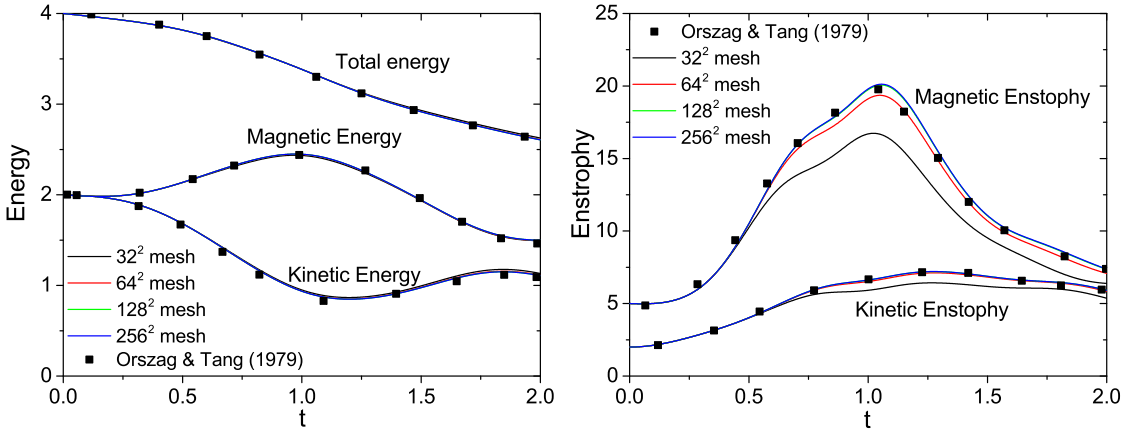

(a) kinetic and magnetic energy (b) kinetic and magnetic enstrophy

Fig. 5. Temporal evolution of: (a) spatially averaged kinetic and magnetic energy, and (b) spatially averaged kinetic and magnetic enstrophy, for the 2D OTV.

Table 3
Comparison of the global maxima of Ω_k and Ω_m at $t=0.5$ and $t=1.0$ for the 2D OTV flow.

t	mesh	Xcompact3d		Dellar (2002) [16]		De Rosis et al. (2021) [25]	
		Ω_k	Ω_m	Ω_k	Ω_m	Ω_k	Ω_m
0.5	32^2	22.61	15.53	-	-	-	-
	64^2	22.43	17.71	-	-	-	-
	128^2	22.84	18.22	22.74	17.96	21.95	16.88
	256^2	22.84	18.26	22.81	18.20	22.59	17.88
	512^2	22.85	18.26	22.84	18.24	22.77	18.15
	1024^2	-	-	-	-	22.82	18.22
1.0	32^2	51.48	33.83	-	-	-	-
	64^2	88.26	43.42	-	-	-	-
	128^2	100.93	46.44	98.98	45.13	76.26	39.62
	256^2	101.06	46.69	100.25	46.30	93.02	44.53
	512^2	101.06	46.70	100.82	46.59	98.42	46.09
	1024^2	-	-	-	-	100.39	46.49

Table 4
The parameters for the 3D OTV case. The reference velocity, length, and magnetism are 1.

Parameter	Value
`mhd_active`	`true`
`mhd_equation`	`induction`
Stuart number	17.54
Magnetic Reynolds number	17.54
Reynolds number	17.54

is excellent. The kinetic enstrophy from all the meshes collapse as it can be seen in Fig. 7 (a). Comparing the relative errors of enstrophy shown in Fig. 7 (b) with the errors of the energy, we can observe that the enstrophy error is an order of magnitude larger than the energy error, meaning that the enstrophy is more sensitive to the spatial resolution. The level of enstrophy errors reduces from approximately 10^{-1} for the simulation with 32^3 mesh nodes to approximately 10^{-3} for the simulation with 128^3 mesh nodes.

To further highlight the difference between the results from different meshes, Fig. 8 compares the global maximum of current density, J_{max}, calculated as, $J_{max} = \max\left[\left(\vec{J}\cdot\vec{J}\right)^{1/2}\right]$, and the max operator returns the peak value within the computational domain. The results from the simulation with 128^3 mesh nodes and 256^3 mesh nodes agree perfectly with the DNS from a high-resolution pseudo-spectral solver performed with a 128^3 mesh nodes [26]; the result from our simulation with 64^3 mesh nodes yields a slightly lower peak at $t=1.16$. Even for the simulation with 64^3 mesh nodes, Xcompact3d still yields superior results when compared to the data of De Rosis et al. [25], obtained with a lattice Boltzmann solver with 128^3 lattice points, showing the advantage of high-order methods in capturing the flow features of a 3D MHD flow. The highest values of J_{max} from the Xcompact3d code are respectively 19.9230, 22.4334, 22.7469 and 22.7571 when the mesh size is gradually increased from 32^3 mesh nodes to 256^3 mesh nodes. Therefore, Xcompact3d converges to the result ($J_{max}=22.7439$) obtained in the reference data generated by a pseudo-spectral solver [26] for the simulation with 128^3 mesh nodes, indicating a similar accuracy for both solutions.

3.3. Laminar two dimensional MHD channel flow

A channel flow bounded by upper and lower walls under an external magnetic field normal to the flow direction is studied in this section. The MHD channel flow is also known as Hartmann flow, which was first analysed by Hartmann and Lazarus in 1937 for the flow of mercury [27]. For a Hartmann flow, the magnetic Reynolds number is typically small, *i.e.*, $Re_m \ll 1$, and the induced magnetic field is negligible. We therefore employ the potential solver for this case. The flow is between two infinite walls positioned at $y=0$ and $y=2$, and driven by a pressure gradient in the x-direction, as sketched in Fig. 9. A periodic condition is applied at both the inflow and outflow planes, and the velocity is enforced to be zero on the walls with a zero wall-normal pressure gradient. A constant magnetic field, $\vec{B}=(0,1,0)$, is applied in the wall-normal direction, inducing an electric current in the fluid, and further leads to a Lorentz force opposing the flow. Consequently, the velocity profile will be changed due to the body force.

The flow parameters are listed in Table 5, in which the Hartmann number, Ha, is defined as,

$$\mathrm{Ha} = B_0 L\sqrt{\frac{\sigma\rho_0}{\nu}} = \sqrt{\mathrm{Re\ N}}. \tag{21}$$

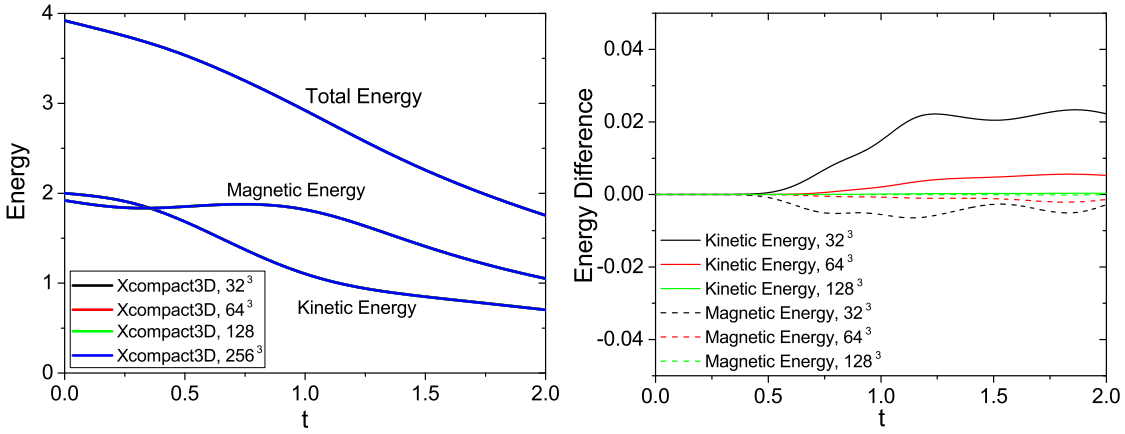

(a) kinetic and magnetic energy (b) Difference to the result from 256^3 mesh

Fig. 6. Temporal evolution of: (a) spatially averaged kinetic and magnetic energy for the 3D OTV, and (b) their difference to the finest mesh solution.

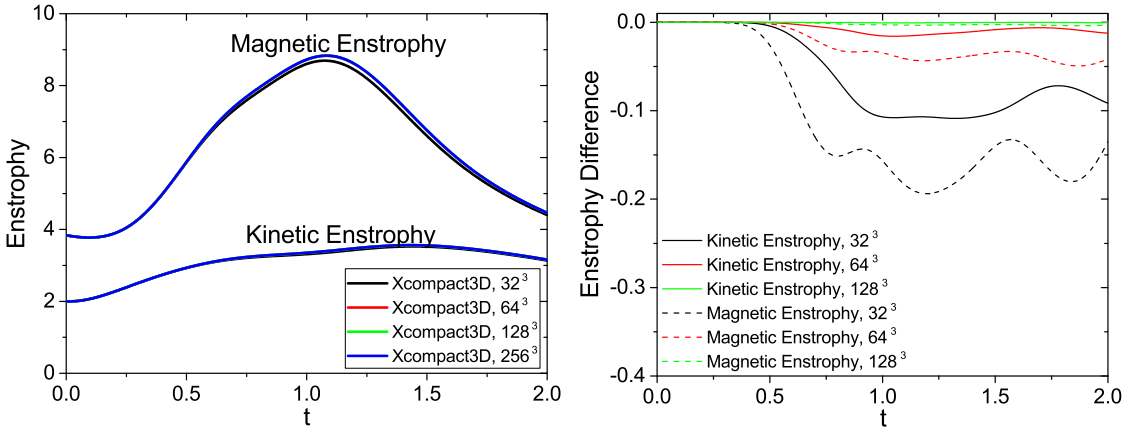

(a) kinetic and magnetic enstrophy (b) difference to the result from 256^3 mesh

Fig. 7. Temporal evolution of: (a) spatially averaged kinetic and magnetic enstrophy for the 3D OTV, and (b) their difference to the finest mesh solution.

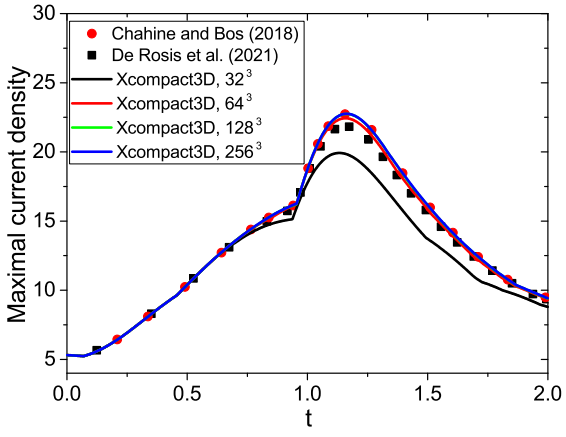

Fig. 8. Temporal evolution of global maxima of current density, J_{max}.

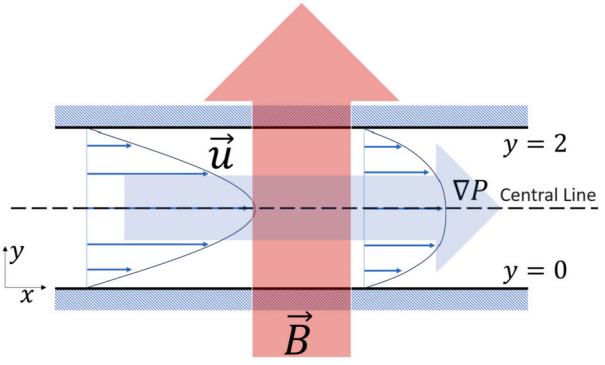

Fig. 9. Sketch of a 2D Hartmann flow.

The reference velocity and length are respectively the bulk velocity, $u_b = \frac{1}{2}\int_0^2 u_x dx$, and the half-height of the channel, h. A uniform pressure gradient is applied in the x-direction to maintain a constant $u_b = 1$.

The computational domain is a 2D rectangle, with only 8 mesh uniformly distributed in the x-direction from 0 to 1, and 129 nodes in the y-direction from 0 to 2. Xcompact3d has the capability of dealing with non-uniform mesh in the y-direction, which is beneficial for the simulation of wall-bounded flows. For this case, the stretching function described in [10] is applied to the nodes in the y-direction so that the resolution is refined near both walls, and the distance of the first node away from the way is $y_1 = 0.00556$.

The simulation starts from a laminar channel flow without MHD, and reaches a steady state after $t = 800L/u_b$, as shown in Fig. 10, in which the friction velocity is defined as, $u_\tau = \sqrt{\frac{\nu}{\mathrm{Re}}\frac{\partial u_x}{\partial y}}$. With a wall-normal magnetic field, the central line velocity is reduced and the skin friction

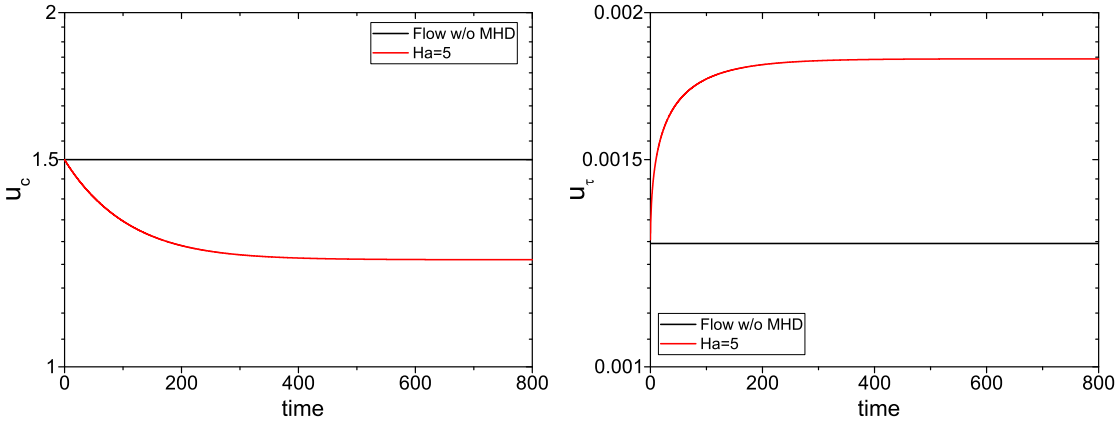

(a) central line velocity (b) friction velocity

Fig. 10. History of the central line velocity and friction velocity for channel flow with and without MHD.

Table 5
Parameters of the laminar channel flow. Re_b is the Reynolds number based on the bulk velocity and half of the channel height.

Parameter	Values
`mhd_active`	`true`
`mhd_equation`	`potential`
Reynolds number	$Re_b = 2800$
Hartmann number	1,5,10

goes up. This is due to the Lorentz force that is trying to slow down the fluid, but a fixed bulk velocity (*i.e.*, the mass flux) is imposed in the simulation. The Lorentz force is larger for the fluids with a higher speed, and consequently, the fluid in the central region of the channel is slowed down, but the fluid's velocity in the near-wall region is increased, leading to a flat velocity profile and an increased skin-friction.

The comparison of velocity profiles at different Hartmann numbers is presented in Fig. 11, in which the analytical solution is obtained via the following formula [28],

$$u = \frac{\mathrm{Re}_\tau \cdot u_\tau}{\mathrm{Ha} \cdot \tanh(\mathrm{Ha})} \frac{1 - \cosh(\mathrm{Ha} \cdot (y-1))}{\cosh(\mathrm{Ha})}, \tag{22}$$

in which $\mathrm{Re}_\tau = u_\tau h/\nu$ is the friction Reynolds number. The flattened velocity profile with an increased Hartmann number can be observed in Fig. 11. Perfect agreements between the results from Xcompact3d and the analytical solution at different Hartmann numbers are confirmed, indicating that the electric potential solver has been correctly applied.

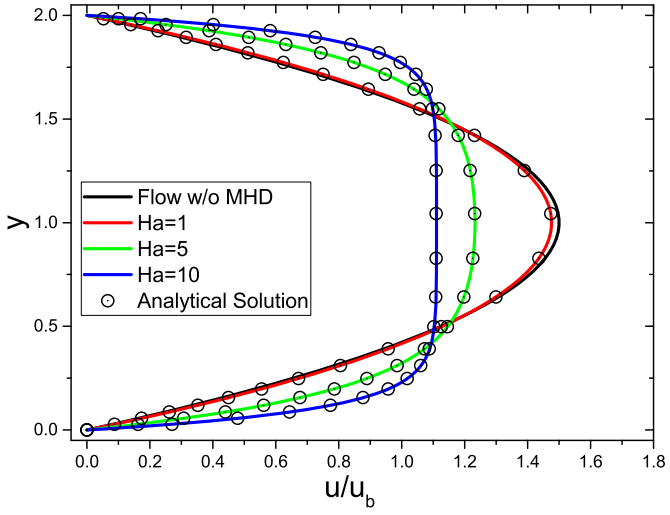

Fig. 11. Comparison of velocity profiles at different Hartmann numbers.

3.4. Turbulent three dimensional MHD channel flow

The performance of our MHD solver is now evaluated for a fully turbulent wall-bounded flow in 3D by looking at the influence of the Hartmann number on wall turbulence. The numerical configuration is a turbulent channel flow, with a $4\pi \times 2 \times 2\pi$ computational domain discretised with a $256 \times 129 \times 192$ mesh nodes. The mesh nodes are uniformly distributed in the $x-$ and z-directions and refined towards the walls in the y-direction. The mesh resolution for the case without MHD is $\Delta x^+ = 7.4$, $\Delta y_1^+ = 0.83$, $\Delta y_m^+ = 6.6$, and $\Delta z^+ = 4.9$, in which the superscript, $+$, stands for variables in wall units and subscripts 1 and m indicate the mesh spacing for the first node away from the wall and the node at the channel centre, respectively. The flow parameters are selected to ease the comparison with the reference data obtained by Nishimura and Kasagi [29], as listed in Table 6.

Table 6
Parameters of the turbulent channel flow.

Parameter	Values
`mhd_active`	`true`
`mhd_equation`	`potential`
Reynolds number	$Re_b = 2305$
Hartmann number	0,4,6,8

Similar to the 2D laminar channel flow case, a uniform pressure gradient is applied in the x-direction to maintain a constant bulk velocity $u_b = 1$. A DNS of a 3D turbulent channel flow without MHD is first conducted up to $t = 1,500h/u_b$, after which the magnetic field is applied. The simulations with MHD are conducted up to $t = 120,000h/u_b$, and the statistics are collected from $t = 90,000h/u_b$ to $t = 120,000h/u_b$.

The time and spatially (x/z-directions) averaged velocity profile and the Reynolds stress in the channel without MHD are compared with previous DNS and experiments in Fig. 12. The operator, $\langle\rangle$, in Fig. 12, denotes a quantity obtained by averaging in time and homogeneous directions, and the superscript, $'$, indicates a fluctuating variable from the mean, as $f = \langle f \rangle + f'$. A good agreement for the velocity profiles against the classic law of wall, the experiment of Eckelmann [30] and the previous DNS of Moser et al. [31] is confirmed. Some differences can be noted on the Reynolds stress profiles between the present DNS and the result of Moser et al. [31], due to the slight difference in Reynolds number. The friction Reynolds number of the present case ($Re_\tau = 150$) is slightly lower than the one obtained in the DNS of Moser et al. ($Re_\tau = 178$). By scaling the vertical coordinate with wall units and channel half-height, we obtain excellent agreements between the two DNSs respectively in the inner and outer regions of the channel, as shown in Fig. 12 (c, d).

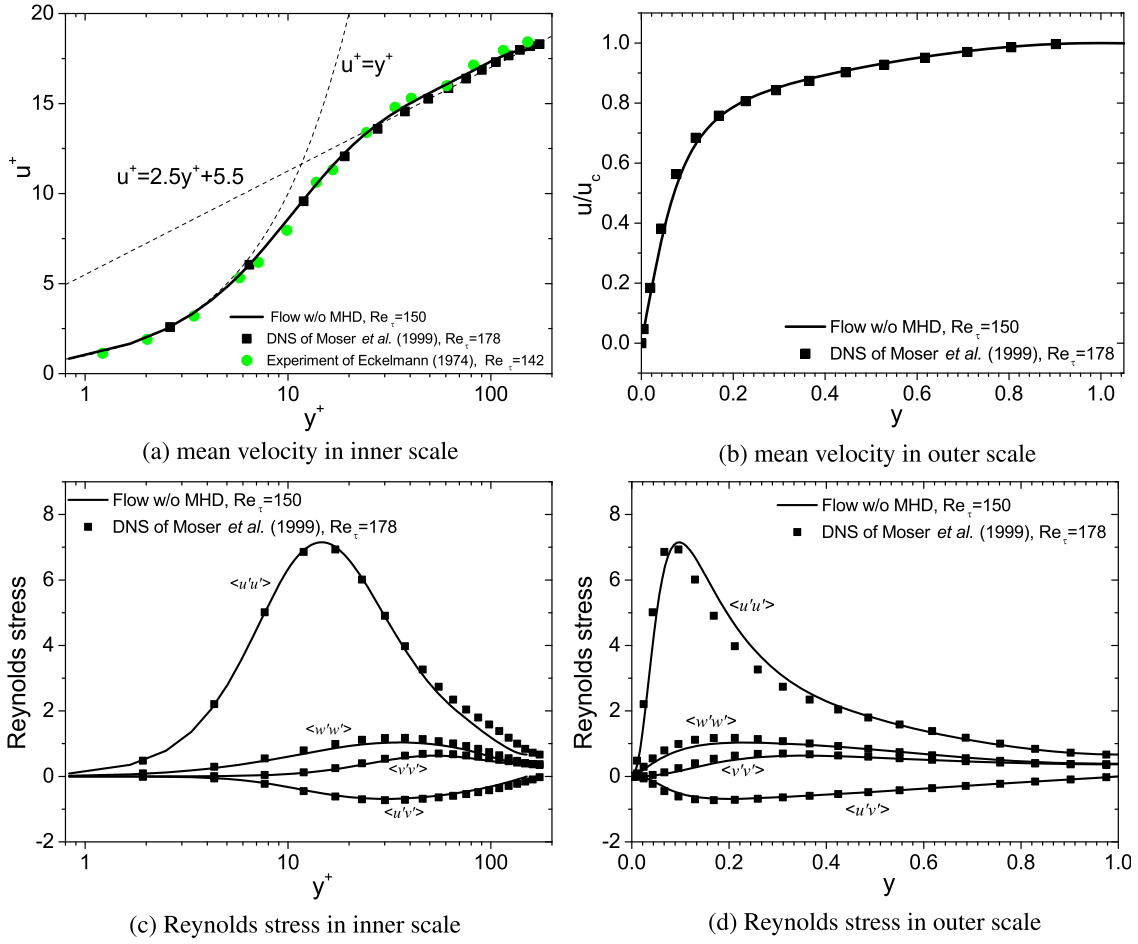

(a) mean velocity in inner scale

(b) mean velocity in outer scale

(c) Reynolds stress in inner scale

(d) Reynolds stress in outer scale

Fig. 12. Mean velocity and Reynolds stress profiles for a conventional turbulent channel flow. The Reynolds stress is normalised with the friction velocity, u_τ^2.

The velocity profiles in the channel flow with vertical magnetic fields at different Hartmann numbers are compared with the DNS database of the THTLab produced by Noguchi and Kasagi [7] in Fig. 13. The magnetic field leads to a lift of the log layer, similar to the velocity profiles in some drag-reducing turbulent flows [32–36]. With the increase of the Hartmann number, the log layer is diminished. The difference between the present DNS and the THTLab data can be seen in Fig. 13 (a), in which the Xcompact3d predicts a slightly higher log layer than the THTLab data. Nonetheless, a good agreement between the two sets of data is observed when the velocity profiles are scaled with bulk velocity in Fig. 13 (b). We can see that with the increase of the Hartmann number, the mean velocity gradually becomes flat, similar to the observation in the laminar channel flow in Fig. 11. When the Hartmann number is increased to $Ha = 8$, the velocity profile collapses to the laminar solution, meaning the flow is relaminarised.

The Reynolds stress profiles are compared with the THTLab data in Fig. 14, from which we can confirm a good agreement between the two sets of data at $Ha = 4$ and $Ha = 6$, although the THTLab data shows slightly higher Reynolds stress. From Fig. 14, we see the suppression of fluctuations from turbulence by the vertical magnetic field, and with the increase of the Hartmann number, lower values of Reynolds stress are obtained. As expected for $Ha = 8$, all the Reynolds stress components are zero, meaning that the flow is fully laminar.

The turbulence structures at the end of the simulations are shown in Fig. 15. The coherent structures are visualised using the Q-criterion, *i.e.*, the iso-surface of the second invariant of the velocity gradient tensor, coloured with the streamwise vorticity, ω_x. The coherent structures in the channel flow present streamwise vortices with arc-shape heads, known as the hairpin or horseshoe structures of wall-bounded turbulence [37,38]. The instantaneous streamwise velocity at the $y^+ = 10$ plain is also shown in Fig. 15. Rich coherent structures are observed in the non-MHD channel flow, and the velocity presents streamwise elongated meandering patterns, known as the streaks [39]. For the cases with non-zero Hartmann numbers, the magnetic field applied in the vertical direction largely suppresses the turbulence structures. We can see the coherent structures become sparser with an increase of Ha, and for $Ha = 8$ we barely see any structures in the channel, which agrees with the relaminarisation of the channel flow at $Ha = 8$ observed above. The velocity streaks also become less energetic with an increase of the Hartmann number. From $Ha = 4$ to $Ha = 6$, the low-speed streaks become wider and less meandering, and no streak can be observed at $Ha = 8$ as the channel flow is fully laminar.

3.5. Computing performance and scalability

The computational cost of the MHD solver is compared with the baseline hydrodynamic solver of the original Xcompact3d for the 3D OTV flow on ARCHER2, the UK supercomputing facility [40]. The full ARCHER2 system is an HPE Cray EX supercomputing system with an estimated peak performance of 28 Pflop/s. The machine has 5,860 compute nodes, each with dual AMD EPYC 7742 64-core processors at 2.25GHz, giving 750,080 cores in total. The interconnect is HPE Cray Slingshot.

The computing cost per time step cost for the different solvers is listed in Table 7. The time is obtained by averaging the total CPU time over 50 time steps. For the data listed in the table, the size of the mesh for each computing core (corresponding to one MPI process) is maintained at 262,144. The corresponding plot for the weak scaling is shown in Fig. 16, from which we can note that the CPU time increases with the

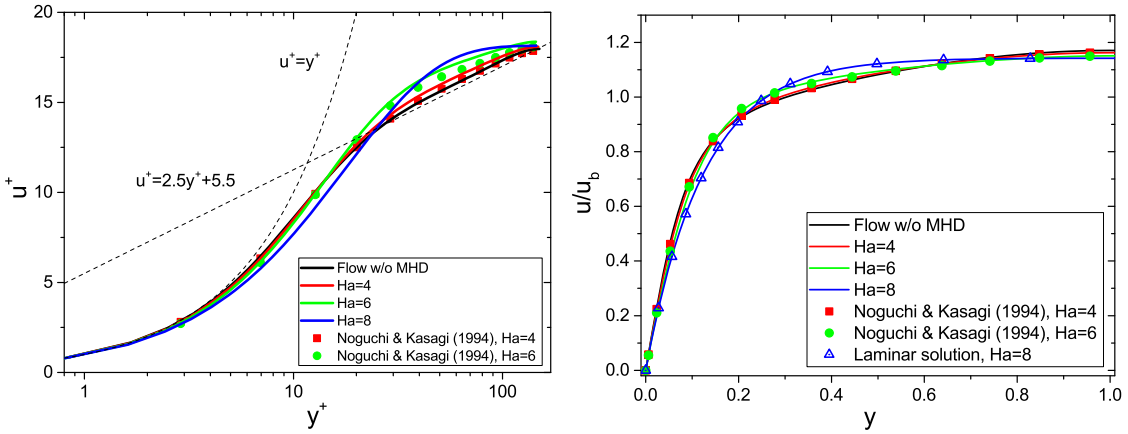

(a) mean velocity in inner scale (b) mean velocity in outer scale

Fig. 13. Mean velocity profiles with different Hartmann numbers.

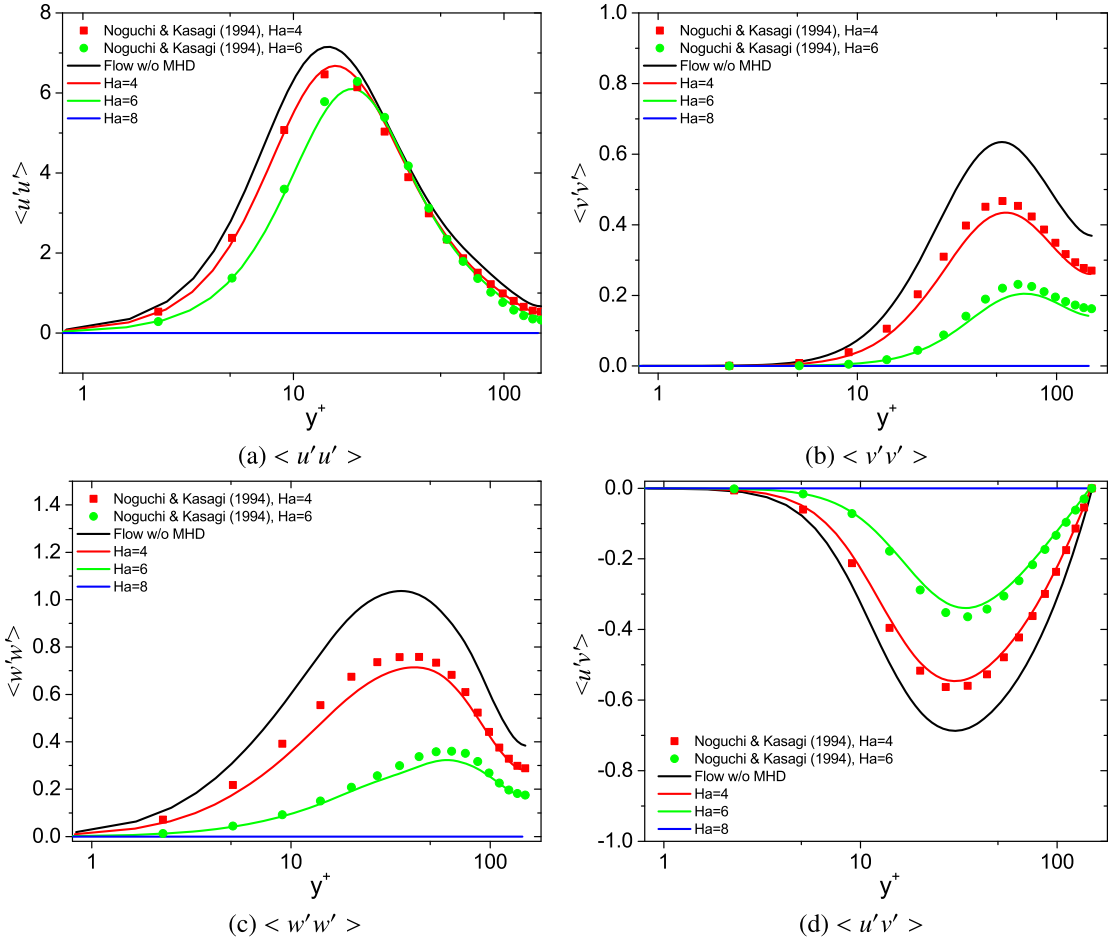

Fig. 14. Reynolds stress profiles for the MHD channel flows. The Reynolds stress is normalised with the local friction velocity, u_τ^2.

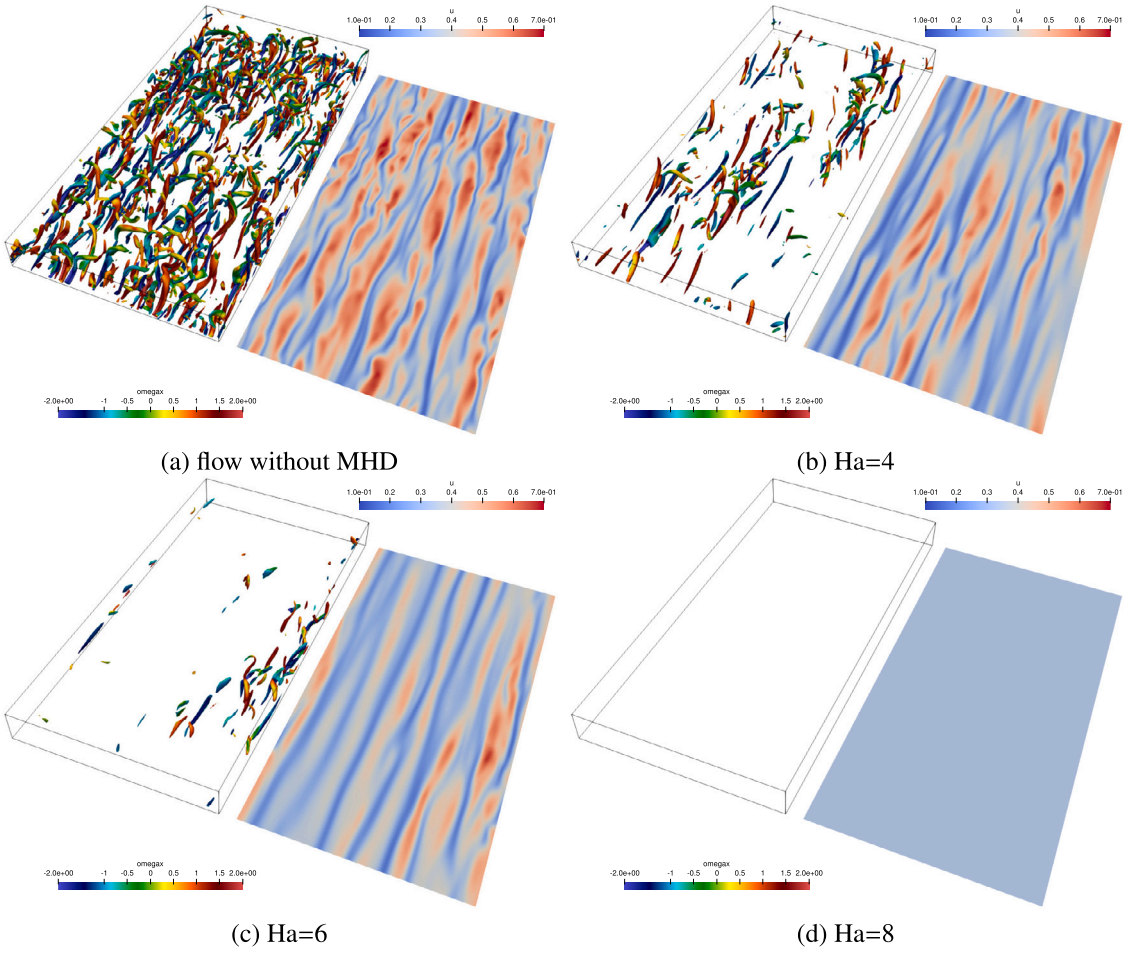

Fig. 15. Turbulence structures in the lower half part of the channel.

Table 7
Computational time (second) per step for the 3D OTV case with different mesh sizes and computing cores.

Number of cores	Mesh size	NS solver	NS+Potential solver	NS+Induction solver
8	128^3	0.54	0.92	1.43
64	256^3	1.44	2.31	3.0
512	512^3	2.15	3.23	5.72
4096	1024^3	2.41	3.56	6.33

number of cores, which is a common phenomenon for parallel computing software. The increase of CPU time gradually stabilises, indicating good scalability.

The ratio of computing times between the MHD solvers and the NS solver is plotted in Fig. 16 (b). It can be seen that the NS+potential solver has a cost per time step about 1.5 times higher than the NS solver alone, while the NS+induction solver has a higher cost, about 2.6 times more than the NS solver alone. The NS solver contains 3 transport equations and 1 Poisson equation, and the NS+potential solver needs to solve one extra 1 Poisson equation. Considering the fact that the Poisson solver is based on a spectral approach, requiring expensive 3D FFTs, the extra cost associated with the potential solver is reasonable. For the induction solver, 3 extra transport equations and 1 extra Poisson equation are needed on top of the NS solver, while the convection terms in the induction equations have more terms than the NS equations. It explains why the NS+induction solver is much more expensive than the NS+potential solver.

To further analyse the scalability of the bew MHD module, the strong scaling for all the solvers is plotted in Fig. 17 with up to 32,768 CPU cores for simulations with up to 1024^3 mesh nodes. It can be seen that the strong scalability for all the solvers is satisfactory for all spatial resolutions, as long as the number of mesh nodes per core is large enough. For the 256^3 simulation, the scalability is excellent with up to 1,024 computational cores and is really poor when using more cores. This is the result of assigning a too small workload to each MPI process, the network latency becoming dominant eventually so that the scalability cannot be improved. However, for a simulation with more mesh nodes (1024^3), the scalability is excellent up to 16,384 computational cores. The key message here is that the potential and induction solvers do not alter the strong scaling of Xcompact3d.

4. In-dept study of the three dimensional MHD Taylor-Green vortex flow

The section is dedicated to the study of the well-known Taylor-Green vortex (TGV) flow in the presence of a magnetic field. The same set of numerical methods as Sec. 3 is used to study the problem, *i.e.*, the sixth-order compact central scheme for the spatial discretisation and the third-order Runge-Kutta scheme for the time advancement. The TGV problem involves the temporal and spatial evolution of two pairs of counter-rotating vortices initially defined as,

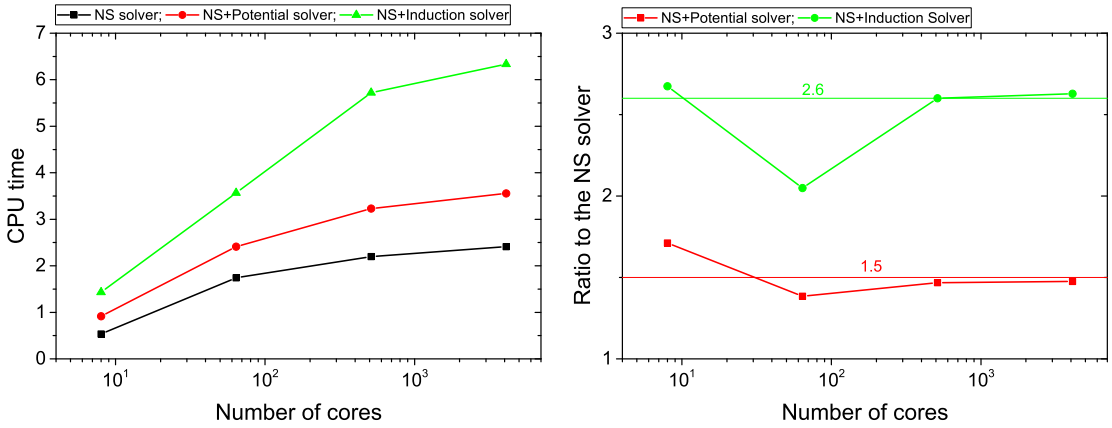

(a) CPU time per step (b) Ratio to the NS solver

Fig. 16. Weak scaling of the MHD and NS solvers.

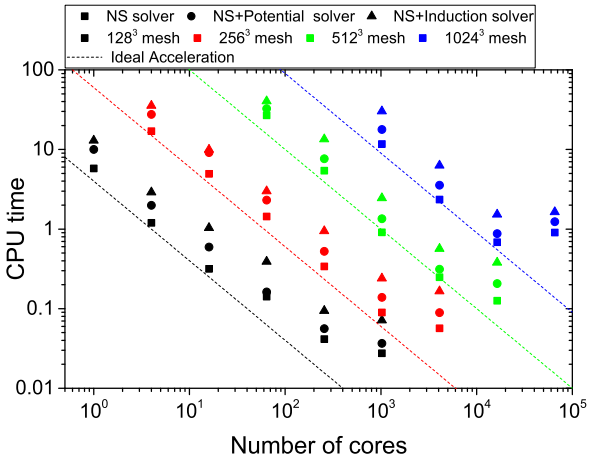

Fig. 17. Strong scaling of the MHD and NS solvers.

$$
\begin{aligned}
u_x &= U_0 \sin(x/L)\cos(y/L)\cos(z/L),\\
u_y &= -U_0 \cos(x/L)\sin(y/L)\cos(z/L),\\
u_z &= 0,
\end{aligned}
\tag{23}
$$

in a 3D $(2\pi L)^3$ periodic cube domain [41] (periodic boundary conditions). The reference velocity, U_0, and reference length, L, are set to 1 for this study.

For a pure hydrodynamic problem, the kinetic energy, E_k, continuously decays due to the viscous dissipation. But the enstrophy, Ω_k, as a measurement of vortical energy, tends to initially grow due to the nonlinear vortex stretching (depended on Reynolds number), and then decay due to viscosity [42]. The TGV flow is commonly used as a benchmark for testing the accuracy of numerical methods and CFD software [43,44], as the level of enstrophy and dissipation rate is sensitive to the mesh and numerical resolution.

Few studies have been devoted to a TGV flow with a magnetic field (*i.e.*, TGV-MHD flow), as most of the research on homogeneous MHD turbulence has been focused on the OTV flow. The evolution of flow structures is highly related to the initial distribution of the magnetic field, even if the initial velocity field is the same. Breyiannis and Valougeorgis [45] used the 3D TGV-MHD flow to validate their lattice Boltzmann solver, using an initial magnetic field defined as,

$$
\vec{B} = B_0 \begin{bmatrix} \sin(x/L)\sin(y/L)\cos(z/L) \\ \cos(x/L)\cos(y/L)\cos(z/L) \\ 0 \end{bmatrix}.
$$

This initial magnetic field also presents two pairs of vortical structures, similar to the velocity field. They observed the well-known mechanism of energy transfer between magnetic and hydrodynamic fields and enhanced dissipation through the creation of currents and vorticity. Vahala et al. [46] adopted the usual initial velocity field from the TGV flow combined with the usual initial magnetic field from the OTV flow,

$$
\vec{B} = B_0 \begin{bmatrix} -2\sin(2y/L)\sin(z/L) \\ 2\sin(x/L) + \sin(z/L) \\ \sin(x/L) + \sin(y/L) \end{bmatrix},
$$

to test their lattice Boltzmann algorithms. They have also observed a strong energy exchange from kinetics to magnetism, and a rapid rise in the magnetic enstrophy. Pouquet et al. [47] and Krstulovic et al. [48] analysed the TGV-MHD flow with yet another type of initial magnetic fields, *i.e.*,

$$
\vec{B^I} = B_0 \begin{bmatrix} \cos(x/L)\sin(y/L)\sin(z/L) \\ \sin(x/L)\cos(y/L)\sin(z/L) \\ -2\sin(x/L)\sin(y/L)\cos(z/L) \end{bmatrix},
$$

$$
\vec{B^A} = B_0 \begin{bmatrix} \cos(2x/L)\sin(2y/L)\sin(2z/L) \\ \cos(2x/L)\sin(2y/L)\sin(2z/L) \\ 0 \end{bmatrix},
$$

$$
\vec{B^C} = B_0 \begin{bmatrix} \sin(2x/L)\cos(2y/L)\cos(2z/L) \\ \cos(2x/L)\sin(2y/L)\cos(2z/L) \\ -2\cos(2x/L)\cos(2y/L)\sin(2z/L) \end{bmatrix},
$$

representing insulating, alternate insulating, and conducting boundary conditions, respectively. Pouquet et al. [47] reported that the dynamics of the three cases were different, even though the initial conditions had the same energy, the same equipartition between kinetic and magnetic energy, the same zero magnetic helicity, the same weak correlation between the velocity and the magnetic field, and the same type of structures in the current and vorticity, with sheets and rolls. For the insulating condition, the magnetic quantities are stronger than kinetic and enstrophy variables, and for the alternate insulating case, the kinetic and magnetic variables are close to being in balance, but for the conducting condition, the kinetic quantities dominate.

In the present section, we provide a new benchmark with an original set of initial conditions for the MHD quantities. The initial velocity field is defined classically by Eq. (23), but the magnetic field is decomposed into enforced and induced fields with,

$$
\vec{B} = \vec{\mathbb{B}} + \vec{b},
\tag{24}
$$

Table 8
The parameters for the 3D TGV-MHD case. The reference velocity, length, and magnetic field are 1.

Case	Stuart number	Reynolds number	Magnetic Reynolds number	mesh
1	100	100	100	64^3
2	7200	7200	7200	512^3

in which the enforced magnetic field is not updated during the simulation and normal to the initial velocity field as, $\vec{\mathbb{B}} = \begin{bmatrix} 0 \\ 0 \\ 1 \end{bmatrix}$, for this case, and the initial induced magnetic field is zero as, $\vec{b} = \begin{bmatrix} 0 \\ 0 \\ 0 \end{bmatrix}$.

The induction equations (Eq. (2)) are modified with fluctuating induction equations as follows:

$$\begin{aligned}\frac{\partial \vec{b}}{\partial t} =& \frac{1}{2}\left\{\left[\left(\vec{\mathbb{B}}+\vec{b}\right)\cdot\nabla\right]\vec{u}+\nabla\left[\left(\vec{\mathbb{B}}+\vec{b}\right)\otimes\vec{u}\right]\right\} \\ &-\frac{1}{2}\left\{\left(\vec{u}\cdot\nabla\right)\left(\vec{\mathbb{B}}+\vec{b}\right)+\nabla\left[\vec{u}\otimes\left(\vec{\mathbb{B}}+\vec{b}\right)\right]\right\} \\ &+\frac{1}{\mathrm{Re}_\mathrm{m}}\nabla^2\left(\vec{\mathbb{B}}+\vec{b}\right). \end{aligned} \tag{25}$$

This kind of setup could minimise the interference of the initial magnetic field to the evolution of flow structures, as the initial magnetic energy is zero without any structures. Physically, this case can be seen as a model describing the evolution of turbulence in a conductive fluid under an external magnetic source.

Two cases are analysed in this section, a low Reynolds number case and a high Reynolds number case, whose parameters are listed in Table 8. The Reynolds number and the magnetic Reynolds number always are kept the same in a simulation, so that the magnetic Prandtl number, ν/η is always 1. The Stuart number is also set to the same value as the Reynolds number. For the case with a low Reynolds number, dissipation dominates the flow, suppressing the nonlinear interactions between flow structures. But, for the second case with a high Reynolds number, the nonlinear effect is strong enough for the flow to evolve into turbulence-like structures.

4.1. TGV-MHD flow at a low Reynolds number

The statistics for the first case with $\mathrm{Re} = \mathrm{Re}_\mathrm{m} = 100$ are shown in Fig. 18, in which the kinetic and magnetic energy and entropy are defined by replacing $\vec{B}$ with $\vec{b}$ in Eq. (18). The kinetic and magnetic dissipation rates are respectively defined as,

$$\begin{aligned}\epsilon_k &= \frac{1}{\mathrm{Re}}\left\langle\frac{1}{2}\left(\frac{\partial u_i}{\partial x_j}+\frac{\partial u_j}{\partial x_i}\right)^2\right\rangle, \\ \epsilon_m &= \frac{1}{\mathrm{Re}_\mathrm{m}}\left\langle\frac{1}{2}\left(\frac{\partial b_i}{\partial x_j}+\frac{\partial b_j}{\partial x_i}\right)^2\right\rangle. \end{aligned} \tag{26}$$

The strong oscillations of all the kinetic and magnetic statistics can be seen in Fig. 18, indicating an intense two-way energy transfer between kinetic and magnetic fields. The phase difference between kinetic statistics and magnetic statistics is half of the oscillating period, and almost all the energy is transferred between kinetic and magnetic fields during a period. Stretching of magnetic field lines is responsible for the conversion of kinetic energy into magnetic energy. As field lines are stretched due to convection by the fluid, the magnetic field strength increases due to the conservation of magnetic flux. The Lorentz force is responsible for converting magnetic energy into kinetic energy and accelerates the fluid as the magnetic field strength increases. This cycle repeats with an observed frequency of $1/\pi$.

The total energy presents a monotonic decay, but the decay rate is much slower than the TGV without MHD, as shown in Fig. 18 (a). The TGV without MHD presents a clear rise of enstrophy and dissipation rate at $t \approx 5$, which is attributed to the nonlinear vortical interaction. However, such a peak is not noticeable from the total quantities for the MHD case. This suggests that the nonlinear interactions of vortical structures are possibly suppressed by the magnetic field.

For the pure hydrodynamic case (no MHD), from the instantaneous flow structures visualised with the Q-criterion in Figs. 19 (a) and 19 (b-c), we observe the evolution of 3D structures from the initial 2D vortices. The initial streamlines show 2D parallel circles aligned in the z-direction. These evolve into 3D spiralling structures, shown at t =5 and 10. The coherent structures evolve from the initial drum-like structures into 3D rod-like structures, similar to the coherent structures commonly observed in isotropic turbulence [49].

For the TGV flow under a magnetic field, the flow structures evolve differently, as shown in Figs. 20, in which the evolution of flow structures and streamlines within one oscillating period (t = 3.21 to 6.32) is presented. At $t = 3.21$, when the kinetic energy reaches a peak, the streamlines are still present as 2D parallel circles rotating in the z-direction, similar to the initial flow field. The streamlines in the upper and lower parts of the subdomain have opposite rotating directions. At $t = 4.83$, the kinetic energy reduces to a local valley, and we see the main rotating direction changes to x/y-directions. This can be explained as the majority of the kinetic energy has been transferred to magnetic, and the residual motions tend to be randomly directed. The coherent structures have an egg-like shape instead of a rod-like shape as observed the non-MHD flow. At $t = 6.32$, the kinetic energy is increased to another peak (Fig. 18), and a similar flow pattern as $t = 3.21$ is also recovered, but the rotating directions of the streamlines in the upper and lower parts of the subdomain are flipped.

The magnetic coherent structures at $t = 3.21$, 4.83 and 6.32 are visualised in Figs. 21, using the iso-surface of electric current strength, $|J|$, and the magnetic field lines. We observe similar patterns as for the flow structures at different times in the simulation. At $t = 3.21$, when most of the magnetic energy has been converted to kinetic energy, we see that the magnetic structure have an egg-like shape with magnetic lines mainly rotating towards the x/y-directions. At $t = 4.83$, the magnetic energy reaches a peak, and we can see spiralling magnetic lines aligned in the z-direction around a drum-like structure, similar to the flow structures at the peak kinetic energy points shown in Fig. 20 (a,c). The magnetic lines in the upper and lower parts of the subdomain have opposite rotating directions, and they are also connected through the centre of the domain. At $t = 6.32$, when the magnetic energy reaches a local minimum again, we can see both the magnetic coherent structures and magnetic field lines have recovered the same state as they were at $t = 3.21$.

Therefore, for the present TGV-MHD flow at $\mathrm{Re} = \mathrm{Re}_\mathrm{m} = 100$, the flow and magnetic fields behave similarly, and the enforced magnetic field, $\vec{\mathbb{B}}$, acts like a converter to exchange kinetic and magnetic energies. The flow structures and magnetic structures are also very similar to each other and they are well preserved during the kinetics-magnetism oscillations.

4.2. TGV-MHD flow at a high Reynolds number

The temporal evolution of key statistics of the TGV-MHD flow at $\mathrm{Re} = \mathrm{Re}_\mathrm{m} = 7200$ is presented in Fig. 22, from which we shall see a different evolution when compared to the low Reynolds number case, as the nonlinear effect increases with the Reynolds number. A DNS of a conventional TGV flow at $\mathrm{Re} = 1600$ is conducted with a 256^3 mesh as a reference, and even if the Reynolds number is lower, this no-MHD

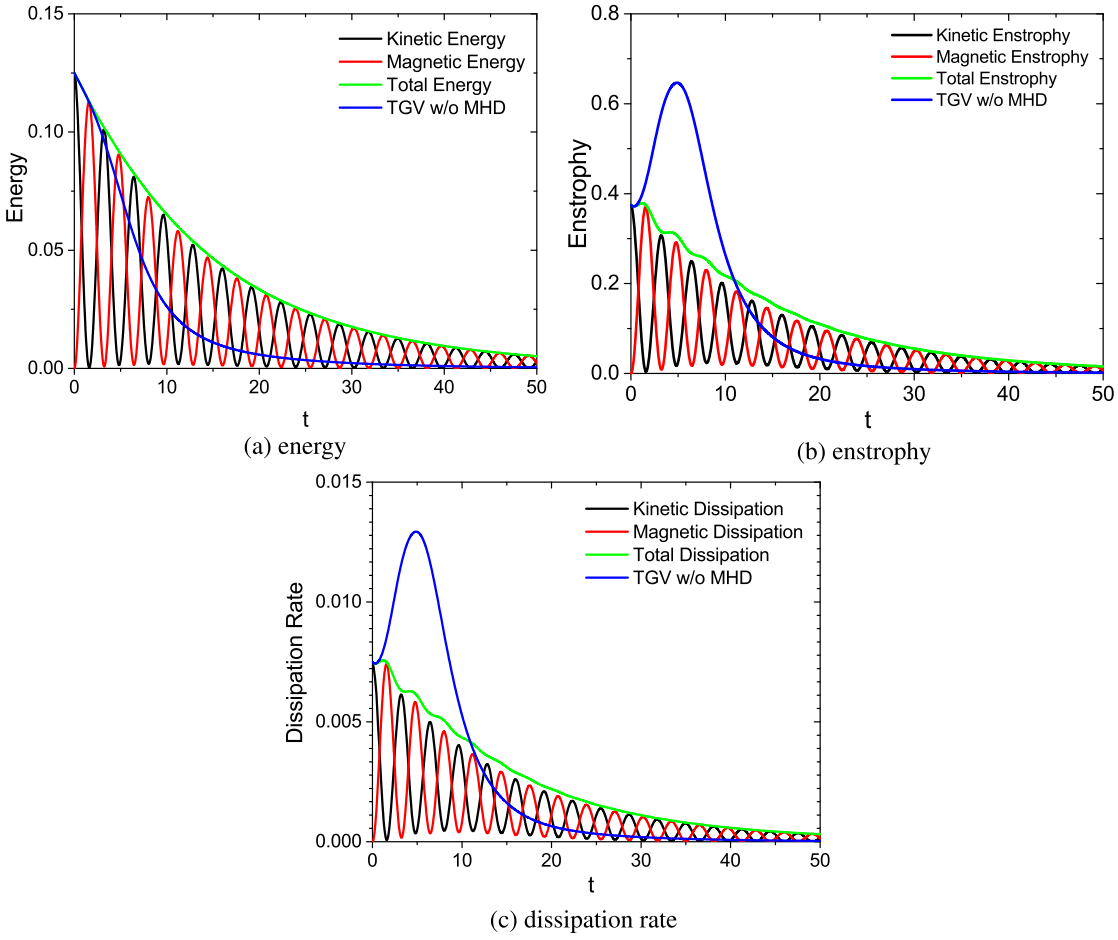

Fig. 18. Temporal evolution of key statistics for the 3D TGV-MHD flow with $Re = 100$.

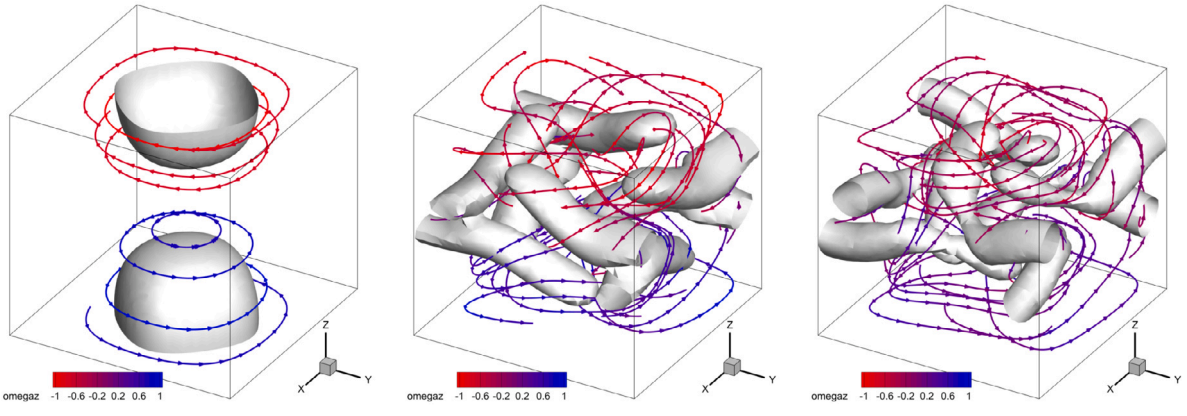

Fig. 19. Flow coherent structures for the TGV case at $Re = 100$ without MHD, visualised with the Q-criterion. The streamlines are coloured with the z-vorticity. Only 1/8 of the domain is shown.

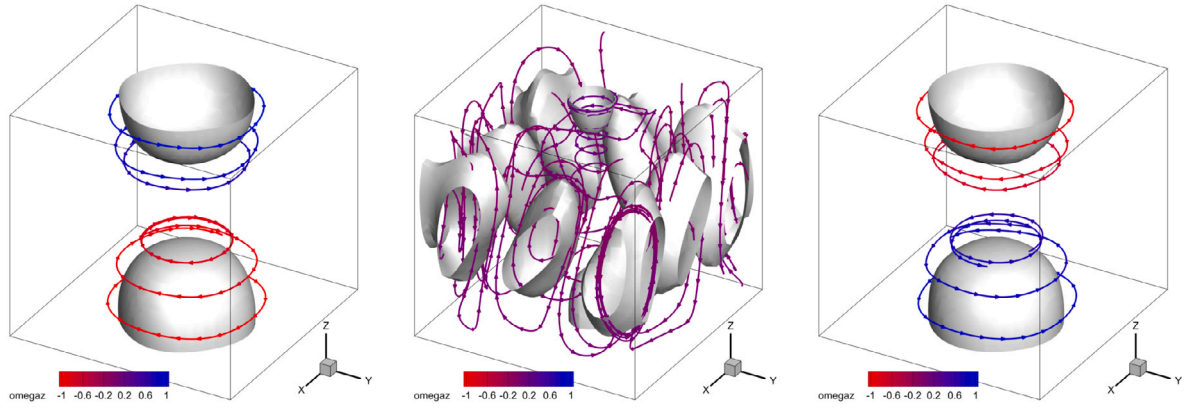

Fig. 20. Flow coherent structures for the MHD-TGV case at $Re = 100$ and $Re_m = 100$. Only 1/8 of the domain is shown, using the same visualisation method as Figs. 19.

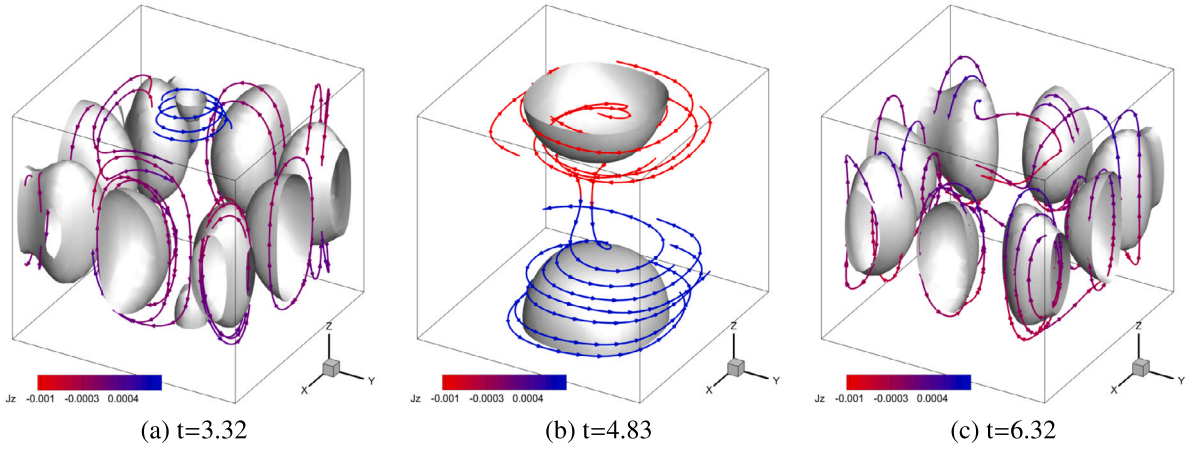

Fig. 21. Magnetic coherent structures for the MHD-TGV case at $Re = 100$ and $Re_m = 100$. The coherent structures are visualised with an iso-surface of current strength, $|J|$. The magnetic field lines are coloured with J_z. Only 1/8 of the domain is shown.

case has a similar level of enstrophy with the TGV-MHD flow, hence it is relevant for comparison.

The energy is still highly oscillatory between kinetic and magnetic energies, and the total energy also presents a monotonic decay due to the diffusion terms from both momentum and magnetic equations. The total energy decay rate is still much lower than the TGV flow without MHD, indicating that the magnetic field slows down the energy diffusion. The decay rate of the total energy is suddenly increased after $t = 30$, which can be explained by the increased dissipation due to the small-scale structures generated by nonlinear effects. It is also worth noting that at the beginning of the evolution, the majority of the energy has been transferred between kinetic and magnetic fields, similar to the low Reynolds number case, but comparatively more energy is preserved for the later cycles. The amplitude of energy oscillation gets smaller with time, especially after $t = 30$. This can be explained as the generation of 3D structures due to the enhanced nonlinear effect leaks the energy from the major rotating direction (*i.e.*, z-direction) to other directions, obstructing the energy transfer under the enforced magnetic field in the z-direction.

The sudden increase of enstrophy and dissipation rate can be seen clearly in Fig. 22 (b, c), and the peaks of both kinetic enstrophy and magnetic enstrophy are reached around $t = 32$, which agrees well with the sudden acceleration of the energy decay rate. This sudden increase of enstrophy means an increase of velocity gradient, which is normally caused by the generation of turbulence-like structures through the nonlinear interaction, *e.g.*, vortex stretching. Compared to the TGV without MHD at a lower Reynolds number ($Re = 1600$), the enstrophy peaks are reached at a significantly later time, which again shows the magnetic field slows down the nonlinear effect in terms of generating 3D flow structures. However, after the peaks are reached, the decay of enstrophy is also slower than the conventional TGV flow.

According to the vorticity and electric current density strength at $t = 50$ shown in Fig. 23, the flow and magnetic fields are highly non-isotropic. Both the flow and magnetic fields present z-direction elongated structures as a result of the enforced magnetic field. Symmetrical patterns are observed for ω_z and J_z on the $x - y$ plain, meaning the flow has not reached a turbulent state, even though many small-scale structures can be seen. It also means that potential numerical errors cannot be seen in this flow obtained with Xcompact3d, as otherwise the symmetry would be broken by the amplification of numerical errors. Both the streamlines and magnetic lines present a swirling pattern, with a large vortex in the middle surrounded by smaller eddies. However, a visual inspection of the flow in Fig. 23 (c), reveals that the vortical structures present a cascade-like pattern. The biggest vortex is seen in the middle, and smaller eddies with different sizes are observed around the central big vortex, describing a 2D scenario of vortex breakdown. From the magnetic field lines in Fig. 23 (d), we only observe a central large vortex and some very small eddies near the edges, lacking vortices with intermediate sizes.

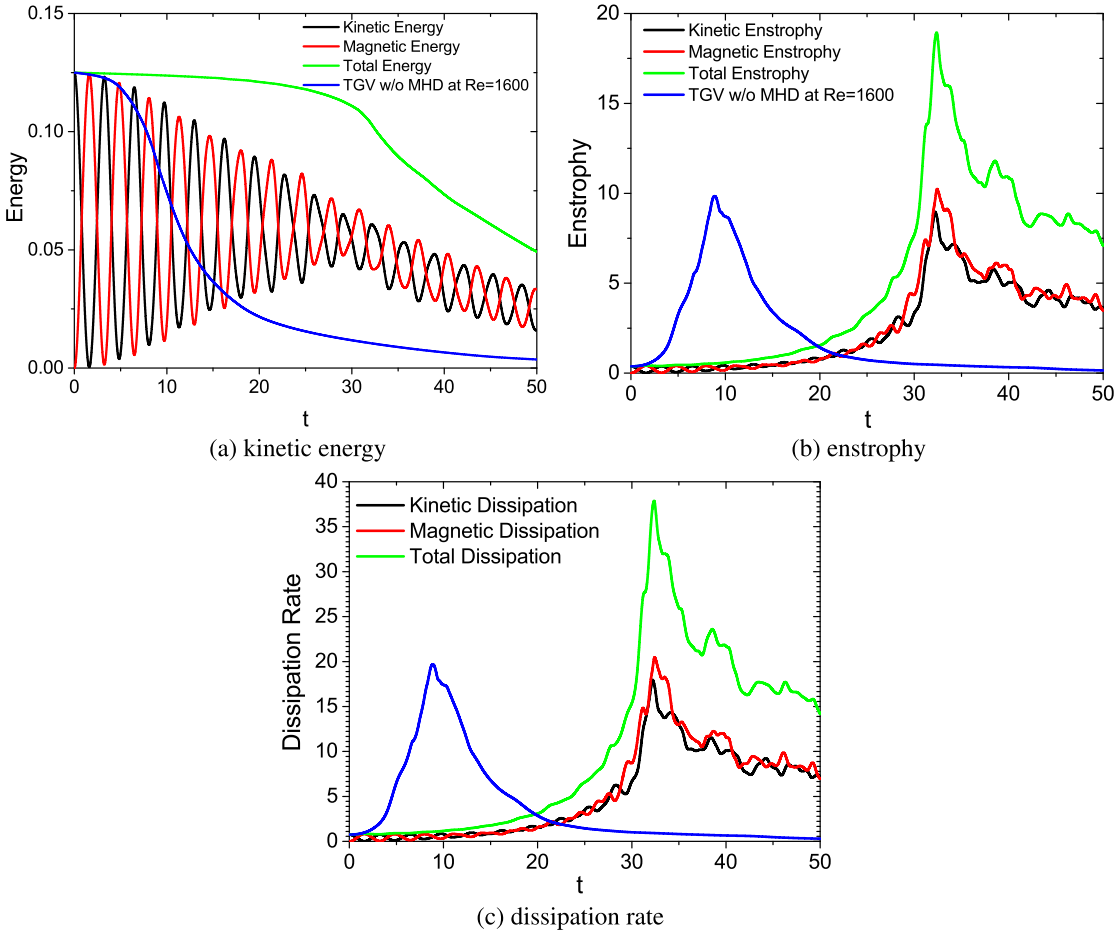

Fig. 22. Temporal evolution of key statistics for the TGV-MHD flow at $Re = 7200$. The results of a non-MHD TGV at $Re = 1600$ are plotted for comparison. For a better comparison, the dissipation rates in (c) are scaled with Reynolds numbers, *i.e.*, $\epsilon_k Re$ and $\epsilon_m Re_m$.

The coherent structures at $t = 50$ are shown in Fig. 24, in which the flow structures are still visualised using Q-criterion coloured with z-vorticity. Rich tube-like structures can be observed in Fig. 24 (a), and these structures are all aligned in the z-direction with positive and negative z-vorticity. The enforced magnetic field tends to adjust the flow structure towards its direction. The coherent structures of conventional TGV flow at $Re = 1600$ is also presented in Fig. 24 (c) for a comparison, and we can observe a huge difference between TGV and TGV-MHD flow. The coherent structures in a conventional TGV flow present randomly oriented worm-like structures, similar with those observed in isotropic turbulence.

The magnetic structures are visualised in Fig. 24 (b), using the isosurfaces of the second invariant of the magnetic gradient tensor, Q_b. The magnetic structures are also z-direction oriented. A detailed inspection of these structures in Fig. 25 (b) reveal that the isosurfaces of Q_b present feather-like structures, rather than tube-like. This agrees with the magnetic field mainly generating sheet-like structures in an MHD flow. From Fig. 25 (a), we also observe locally spiralling streamlines around the tube-like structure, but the magnetic field lines present a different pattern, with some large-scale swirls. This agrees with the observation in Fig. 23.

5. Summary and concluding remarks

In this paper, we introduced a high-order finite-difference solver integrated into the Xcompact3d framework, specifically designed for direct numerical simulations (DNS) of magnetohydrodynamic (MHD) turbulence. The MHD module leverages 3D Fast Fourier Transforms, sixth-order compact finite-difference schemes, and a direct spectral Poisson solver to efficiently handle both induction and potential-based MHD equations on CPU-based supercomputers. The solver was rigorously validated against benchmark cases such as the Orszag-Tang vortex and MHD channel flows, demonstrating its accuracy and robustness in capturing complex MHD phenomena.

Our findings indicate that the Xcompact3d MHD module maintains the scalability of the original framework, ensuring efficient performance on modern high-performance computing clusters. The module shows excellent weak and strong scaling capabilities, making it suitable for large-scale simulations. The computational cost analysis revealed that the MHD solvers are computationally efficient, with the potential solver being only 1.5 times and the induction solver 2.6 times more expensive than the original Navier-Stokes solver per timestep. The module's ability to solve MHD problems at different scales, ranging from weak to strong magnetic fields, makes it a versatile tool for research in both engineering and astrophysics, *e.g.*, the dynamo problems.

Furthermore, we presented new insights into the evolution of the Taylor-Green vortex under an external magnetic field across different flow regimes. The results highlighted the solver's capability to accurately capture the intricate dynamics of MHD turbulence, including energy transfer between kinetic and magnetic fields, as well as the development of turbulence-like structures under varying magnetic influences. With increased nonlinear effects at a higher Reynolds number, the energy transfer was less efficient, with some energy leaking in other directions. The enforced magnetic field significantly delayed the blow-up of enstrophy compared to a hydrodynamic TGV flow. The major flow features were still present in the $x - y$planes. The enforced magnetic field stretched the flow structures in the magnetic direction, forming many small-scale tube-like flow structures and feather-like magnetic

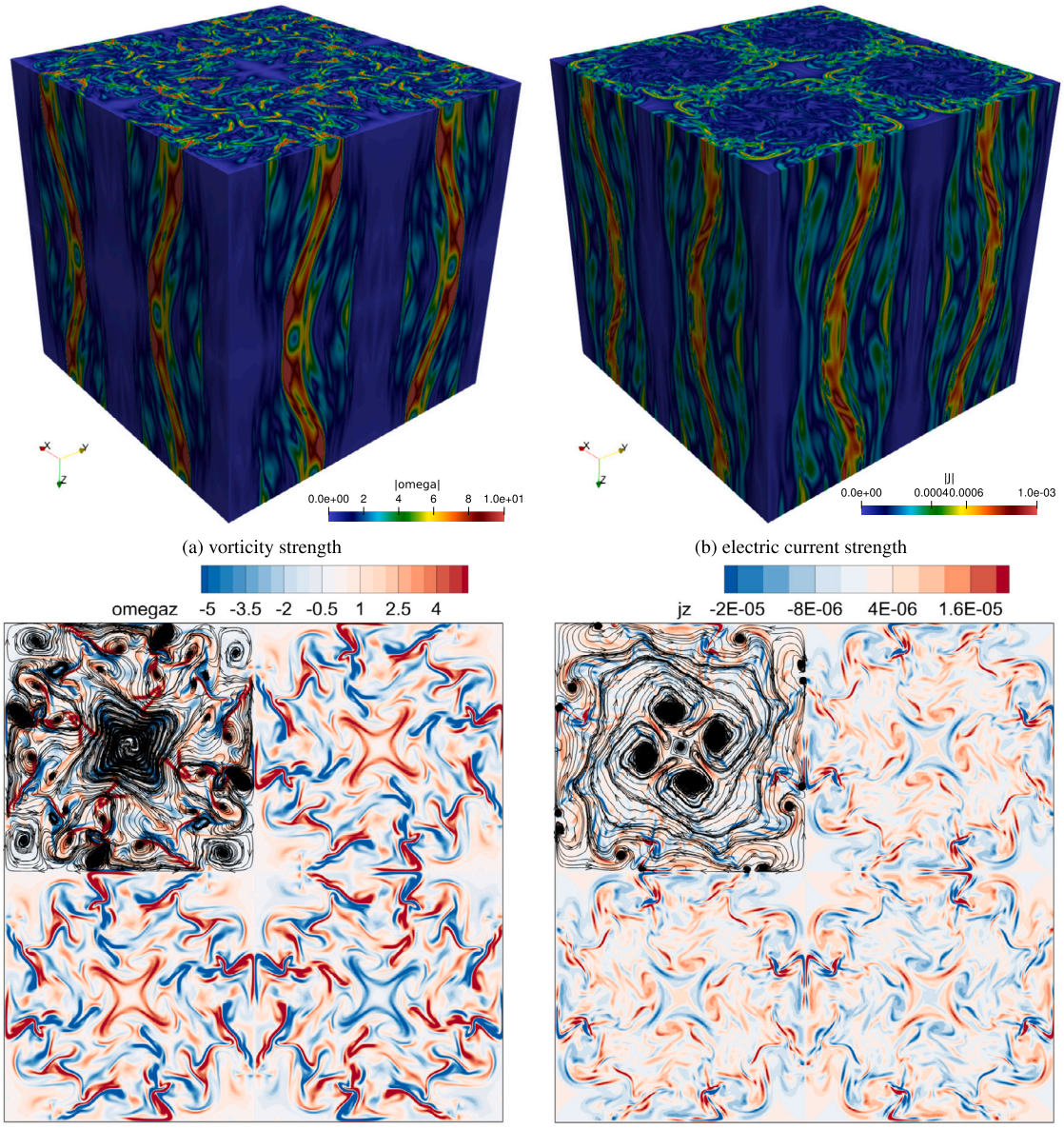

(a) vorticity strength (b) electric current strength

(c) $z-$vorticity with streamlines on the middle $x-y$ plane (d) electric current strength with magnetic lines on the middle $x-y$ plane

Fig. 23. Instantaneous vorticity and electric current fields at $t = 50$ for the MHD-TGV case at $Re = 7200$.

structures. The breakdown of vortices mainly occurred in the $x-y$ planes.

In conclusion, the developed MHD module in Xcompact3d stands as a powerful and efficient tool for the DNS of MHD turbulence, providing significant opportunities for advancing our understanding of MHD flows in various scientific and engineering applications. Future work will focus on extending the solver's capabilities to heterogeneous parallel architectures, including GPUs, and exploring more complex MHD scenarios. We will also test the existing immersed boundary method implemented in Xcompact3d for the provision of different magnetic boundary conditions.

CRediT authorship contribution statement

Jian Fang: Writing – original draft, Visualization, Validation, Software, Methodology, Investigation, Formal analysis, Data curation, Conceptualization. **Sylvain Laizet:** Writing – review & editing, Software, Project administration, Funding acquisition, Data curation, Conceptualization. **Alex Skillen:** Writing – review & editing, Supervision, Project administration, Methodology, Funding acquisition, Conceptualization.

Declaration of competing interest

The authors declare that they have no known competing financial interests or personal relationships that could have appeared to influence the work reported in this paper.

Acknowledgement

The development of the MHD module was funded by the ARCHER2 UK National Supercomputing Service (ARCHER2-eCSE07-3). The authors also gratefully acknowledge the support of the UK Engineering and Physical Sciences Research Council (EPSRC) through the Computational Science Centre for Research Communities (CoSeC), the CCP Turbulence (EP/T026170/1), and the UK Turbulence Consortium (Grant No. EP/R029326/1 and EP/X035484/1). All the simulations were conducted on ARCHER2 and the computing time was awarded through an

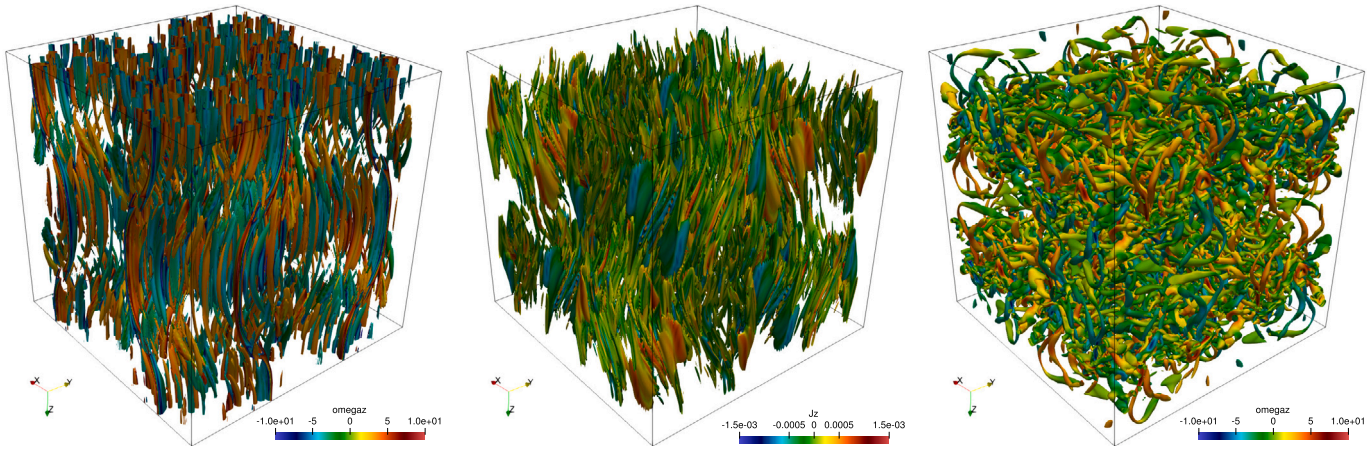

(a) isosurface of Q coloured with ω_z for the TGV-MHD flow at $Re = 7200$ and $t = 50$

(b) isosurface of Q_b coloured with Jz for the TGV-MHD flow at $Re = 7200$ and $t = 50$

(c) isosurface of Q coloured with ω_z for the conventional TGV flow at $Re = 1600$ and $t = 50$

Fig. 24. Flow and magnetic coherent structures of TGV flow with and without MHD.

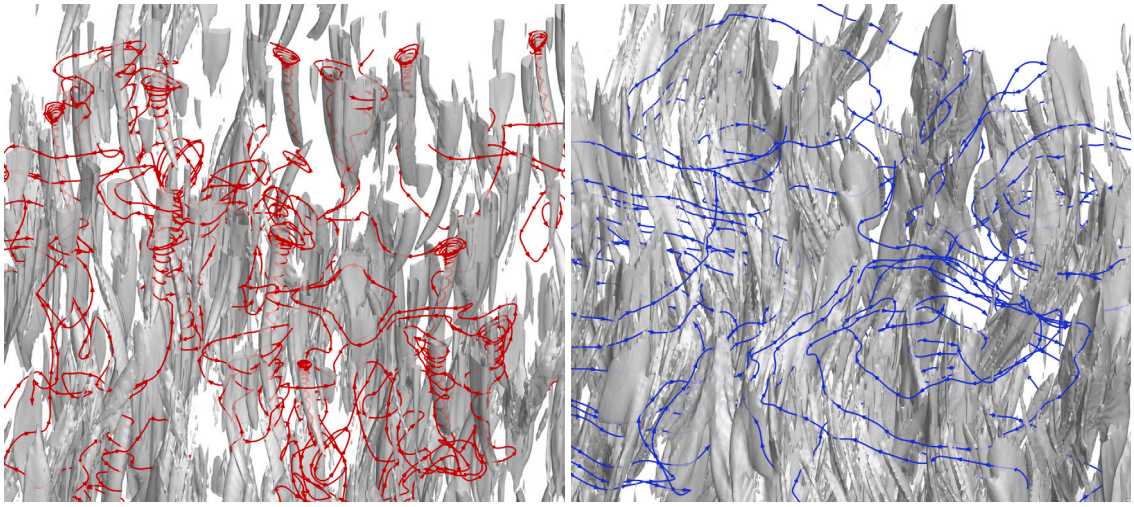

(a) flow structures with streamlines

(b) magnetic structures with magnetic lines

Fig. 25. Zoomed structures for the MHD-TGV case at $Re = 7200$ with streamlines and magnetic lines.

ARCHER2 Pioneer Project. The authors are grateful to Alessandro De Rosis from the University of Manchester for the provision of lattice Boltzmann data and helpful discussions.

Appendix A. Supplementary material

Supplementary material related to this article can be found online at https://doi.org/10.1016/j.cpc.2024.109400.

Data availability

Data will be made available on request.

References

[1] A.N. Kolmogorov, A refinement of previous hypotheses concerning the local structure of turbulence in a viscous incompressible fluid at high Reynolds number, J. Fluid Mech. 13 (1) (1962) 82–85.
[2] S. Galtier, S.V. Nazarenko, A.C. Newell, A. Pouquet, A weak turbulence theory for incompressible magnetohydrodynamics, J. Plasma Phys. 63 (5) (2000) 447–488.
[3] W.-C. Müller, R. Grappin, Spectral energy dynamics in magnetohydrodynamic turbulence, Phys. Rev. Lett. 95 (2005) 114502.
[4] S. Boldyrev, Spectrum of magnetohydrodynamic turbulence, Phys. Rev. Lett. 96 (2006) 115002.
[5] S.A. Orszag, Numerical methods for the simulation of turbulence, Phys. Fluids 12 (12) (1969) II–250–II–257.
[6] C. Canuto, M.Y. Hussaini, A. Quarteroni, T.A. Zang, Spectral Methods: Evolution to Complex Geometries and Applications to Fluid Dynamics, Springer Science & Business Media, 2007.
[7] H. Noguchi, N. Kasagi, Direct numerical simulation of liquid metal MHD turbulent channel flows, Preprint of JSME (940-53) (1994) 365–366.
[8] M. Fontana, P.D. Mininni, O.P. Bruno, P. Dmitruk, Vector potential-based mhd solver for non-periodic flows using Fourier continuation expansions, Comput. Phys. Commun. 275 (2022) 108304.
[9] S.K. Lele, Compact finite difference schemes with spectral-like resolution, J. Comput. Phys. 103 (1992) 16–42.
[10] S. Laizet, E. Lamballais, High-order compact schemes for incompressible flows: a simple and efficient method with quasi-spectral accuracy, J. Comput. Phys. 228 (16) (2009) 5989–6015.
[11] P. Bartholomew, G. Deskos, R.A. Frantz, F.N. Schuch, E. Lamballais, S. Laizet, Xcompact3d: an open-source framework for solving turbulence problems on a cartesian mesh, SoftwareX 12 (2020) 100550.
[12] S. Rolfo, C. Flageul, P. Bartholomew, F. Spiga, S. Laizet, The 2DECOMP&FFT library: an update with new CPU/GPU capabilities, J. Open Sour. Softw. 8 (91) (2023) 5813.
[13] S. Ghosh, M. Hossain, W.H. Matthaeus, The application of spectral methods in simulating compressible fluid and magnetofluid turbulence, Comput. Phys. Commun. 74 (1) (1993) 18–40.
[14] G.A. Blaisdell, E.T. Spyropoulos, J.H. Qin, The effect of the formulation of nonlinear terms on aliasing errors in spectral methods, Appl. Numer. Math. 21 (3) (1996) 207–219.
[15] A.G. Kravchenko, P. Moin, On the effect of numerical errors in large eddy simulations of turbulent flows, J. Comput. Phys. 131 (2) (1997) 310–322.

[16] A. Dedner, F. Kemm, D. Kröner, C.D. Munz, T. Schnitzer, M. Wesenberg, Hyperbolic divergence cleaning for the MHD equations, J. Comput. Phys. 175 (2) (2002) 645–673.
[17] S. Laizet, N. Li, Incompact3d: a powerful tool to tackle turbulence problems with up to o(10^5) computational cores, Int. J. Numer. Methods Fluids 67 (11) (2011) 1735–1757.
[18] R.W. Hockney, A fast direct solution of Poisson's equation using Fourier analysis, J. ACM 12 (1) (1965) 95–113.
[19] P.N. Swarztrauber, The methods of cyclic reduction, Fourier analysis and the FACR algorithm for the discrete solution of Poisson's equation on a rectangle, SIAM Rev. 19 (3) (1977) 490–501.
[20] U. Schumann, R.A. Sweet, Fast Fourier transforms for direct solution of Poisson's equation with staggered boundary conditions, J. Comput. Phys. 75 (1) (1988) 123–137.
[21] J. Williamson, Low-storage Runge-Kutta schemes, J. Comput. Phys. 35 (1) (1980) 48–56.
[22] S.A. Orszag, C.-M. Tang, Small-scale structure of two-dimensional magnetohydrodynamic turbulence, J. Fluid Mech. 90 (1) (1979) 129–143.
[23] D.G. Dritschel, A general theory for two-dimensional vortex interactions, J. Fluid Mech. 293 (1995) 269–303.
[24] H. Li, H. Ki, Simulation of MHD flows using a hybrid lattice-Boltzmann finite-difference method, Commun. Comput. Phys. 4 (2) (2008) 337–349.
[25] A. De Rosis, R. Liu, A. Revell, One-stage simplified lattice Boltzmann method for two- and three-dimensional magnetohydrodynamic flows, Phys. Fluids 33 (8) (2021) 085114.
[26] R. Chahine, W.J.T. Bos, On the role and value of β in incompressible MHD simulations, Phys. Plasmas 25 (4) (2018) 042115.
[27] J. Hartman, F. Lazarus, Hg-Dynamics II: Experimental Investigations on the Flow of Mercury in a Homogeneous Magnetic Field, Mat.-Fys. Medd. 15 (7) (1937).
[28] U. Müller, L. Bühler, Analytical Solutions for MHD Channel Flow, Springer Berlin Heidelberg, Berlin, Heidelberg, 2001, pp. 37–55.
[29] N. Kasagi, M. Nishimura, Direct numerical simulation of combined forced and natural turbulent convection in a vertical plane channel, Int. J. Heat Fluid Flow 18 (1997) 88–99.
[30] H. Eckelmann, The structure of the viscous sublayer and the adjacent wall region in a turbulent channel flow, J. Fluid Mech. 65 (3) (1974) 439–459.
[31] R.D. Moser, J. Kim, N.N. Mansour, Direct numerical simulation of turbulent channel flow up to $Re_\tau = 590$, Phys. Fluids 11 (4) (1999).
[32] K.-S. Choi, J.R. DeBisschop, B.R. Clayton, Turbulent boundary-layer control by means of spanwise-wall oscillation, AIAA J. 36 (7) (1998) 1157–1163.
[33] K.-S. Choi, M. Graham, Drag reduction of turbulent pipe flows by circular-wall oscillation, Phys. Fluids 10 (1) (1998) 7–9.
[34] H. Choi, P. Moin, J. Kim, Direct numerical simulation of turbulent flow over riblets, J. Fluid Mech. 255 (1993) 503–553.
[35] F.C. Li, Y. Kawaguchi, K. Hishida, Investigation on the characteristics of turbulence transport for momentum and heat in a drag-reducing surfactant solution flow, Phys. Fluids 16 (9) (2004).
[36] P. Ricco, M. Skote, M.A. Leschziner, A review of turbulent skin-friction drag reduction by near-wall transverse forcing, Prog. Aerosp. Sci. 123 (2021) 100713.
[37] J.H.F.S. Jeong, Coherent structures near the wall in a turbulent channel flow, J. Fluid Mech. 332 (185) (1997).
[38] M.S. Chong, J. Soria, A.E. Perry, J. Chacin, B.J. Cantwell, Y. Na, Turbulence structures of wall-bounded shear flows found using DNS data, J. Fluid Mech. 357 (1998) 225–247.
[39] S.J. Kline, W.C. Reynolds, F.A. Schraub, P.W. Runstadler, The structure of turbulent boundary layers, J. Fluid Mech. 30 (1967) 741–773.
[40] https://www.archer2.ac.uk/.
[41] G.I. Taylor, A.E. Green, Mechanism of the production of small eddies from large ones, Proc. R. Soc. Lond. Ser. A, Math. Phys. Sci. 158 (895) (1997) 499–521.
[42] M.E. Brachet, Direct simulation of three-dimensional turbulence in the Taylor-Green vortex, Fluid Dyn. Res. 8 (1991) 1–8.
[43] L.T. Diosady, S.M. Murman, Case 3.3: Taylor–Green vortex evolution, in: Case Summary for 3rd International Workshop on Higher-Order CFD Methods, 2015.
[44] A. Mastellone, L. Cutrone, F. Capuano, BS1 - DNS of the Taylor–Green vortex at Re = 1600, in: VII European Congress on Computational Methods in Applied Sciences and Engineering, 2016.
[45] G. Breyiannis, D. Valougeorgis, Lattice kinetic simulations of 3-D MHD turbulence, Comput. Fluids 35 (8–9) (2006) 920–924.
[46] G. Vahala, B. Keating, M. Soe, J. Yepez, L. Vahala, J. Carter, S. Ziegeler, MHD turbulence studies using lattice Boltzmann algorithms, in: 2008 International Sherwood Fusion Theory Conference, Boulder, 2008.
[47] A. Pouquet, E. Lee, M.E. Brachet, P.D. Mininni, D. Rosenberg, The dynamics of unforced turbulence at high Reynolds number for Taylor–Green vortices generalized to MHD, Geophys. Astrophys. Fluid Dyn. 104 (2–3) (2010) 115–134.
[48] G. Krstulovic, M.E. Brachet, A. Pouquet, Forced magnetohydrodynamic turbulence in three dimensions using Taylor-Green symmetries, Phys. Rev. E, Stat. Nonlinear Soft Matter Phys. 89 (4) (2014) 043017.
[49] A. Vincent, M. Meneguzzi, The spatial structure and statistical properties of homogeneous turbulence, J. Fluid Mech. 225 (1) (1991).